

فرایندهای انجماد پیشرفته
(Advanced Solidification Processing)

مدرس: دکتر بهزاد نیرومند

امتحان: روز امتحانات

ارزشیابی: تکالیف (۷-۸ نمره)، امتحان کتبی (۱۳-۱۲ نمره)

مراجع:

- 1- Fundamentals of Solidification, W. Kurz, D.J. Fisher, 4th ed. 1998 (مرجع اصلی درس)
- 2- Solidification Processing, M.C. Flemings, 1974
- 3- Eutectic Solidification Processing: Crystalline and Glassy Alloys, R. Elliott, 1983
- 4- Solidification and Casting, Davies, 1973
- 5- Phase Transformations in Metals and Alloys, D.A. Porter, K.E. Easterling, 1993 (Chapter 4)
- 6- Principles of Solidification, B. Chalmers, 1964
- 7- Materials Science and Technology, Ed. R. W. Cahn, P. Haasen, E.J. Kramer, 1991 (Chapter 1, 2, and 12)
- 8- ASM Handbook (Metals Handbook), ASM, Vol.: 15 (Casting)
- 9- Physical Metallurgy, Ed. R.W. Cahn, P. Haasen, 1983 (Chapter 9 and 28)
- 10- Phase Transformations in Materials, A.K. Jena, M.C. Chaturvedi, 1992 (Chapter 6)
- 11- The Solidification of Metals, A. Ohno, 1976
- 12- An Introduction to the Solidification of Metals, W.C. Winegard
- 13- *Materials Processing during casting, H. Fredriksson و U. Akerlind's 2006.*
+ بقیه کتب و مجموعه مقالات با موضوع Solidification و بسیاری از کتابها و مجموعه مقالات با موضوعات Phase Transformation, Physical Metallurgy, Crystal Growth, Casting, Foundry
- 14- *Fergamon Materials Series, Vol.15, Chapter 13 (Solidification), 2010.*

سرفصل های درس:

- مروری بر مطالب مقطع کارشناسی و بحث های تکمیلی
- Stability of the solid/liquid interface
- Faceted/non-faceted interfaces
- Growth and coarsening of solid particles
- Effects of fluid flow on solidification structure
- Solute redistribution
- Directional solidification
- Eutectic solidification
- Grain refinement
- Macro- and micro-segregation
- Semi-solid processing of alloys
- Effect of pressure on solidification structure
- Rapid solidification
- Solidification processing in microgravity
- Solidification of composites
- Heat transfer in solidification
- Inclusion and porosity formation during solidification
- ...

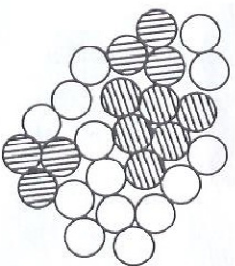


Fig. 4.4 A two-dimensional representation of an instantaneous picture of the liquid structure. Many close-packed crystal-like clusters (shaded) are present.

TABLE 1.1

THE CHANGE IN VOLUME ON MELTING OF SOME COMMON METALS^a

Metal	Crystal structure	Melting point (°C)	Change in volume on melting (%)
Aluminium	f.c.c.	660	+6.0
Gold	f.c.c.	1 063	+5.1
Zinc	h.c.p.	420	+4.2
Copper	f.c.c.	1 083	+4.15
Magnesium	h.c.p.	650	+4.1
Cadmium	h.c.p.	321	+4.0
Iron	b.c.c./f.c.c.	1 537	+3.0
Tin	tet.	232	+2.3
Antimony	rhombohedral	252	-0.95
Gallium	f.c. orthorhombic	631	-3.2
Bismuth	rhombohedral	30	-3.35
Germanium	dia. cubic	271	-5.0
		937	

^a Data from Schneider and Heymer. 1

TABLE 1.3

ENTROPY CHANGES DURING THE HEATING OF SOME COMMON METALS^a

Metal	Change in entropy ^b 298°K to melting point ΔS	Entropy of melting ΔS _m	ΔS _m / ΔS
Cadmium	4.53	2.46	0.54
Zinc	5.45	2.55	0.47
Aluminium	7.51	2.75	0.37
Magnesium	7.54	2.32	0.31
Copper	9.79	2.30	0.24
Gold	9.78	2.21	0.23
Iron	15.50	2.00	0.13

^a Data from Hultgren *et al.*, 3
^b Entropies in cal/mole °K⁻¹.

TABLE 1.2

LATENT HEATS OF MELTING AND VAPORISATION OF SOME COMMON METALS^a

Metal	Crystal structure	Melting point (°C)	Latent heat ^b of melting (L _m)	Boiling point (°C)	Latent heat ^b of vaporisation (L _v)
Aluminium	f.c.c.	660	2.5	2 480	69.6
Gold	f.c.c.	1 063	3.06	2 950	81.8
Copper	f.c.c.	1 083	3.11	2 575	72.8
Iron	f.c.c./b.c.c.	1 536	3.63	3 070	81.3
Zinc	h.c.p.	420	1.72	2 75	22.4
Cadmium	h.c.p.	321	1.53	765	16.0
Magnesium	h.c.p.	650	2.08	1 103	15.6
					32.0
					15.4

^a Data from Smithells, 2
^b Latent heats in kcal/mol⁻¹.

TABLE 1.4

COMPARISON OF STRUCTURAL DATA FOR LIQUID AND SOLID METALS OBTAINED BY DIFFRACTION^a

Metal	Liquid atomic separation	liquid co-ordination number	Solid atomic separation	Solid co-ordination number
Aluminium	2.96	10-11	2.86	12
Zinc	2.94	11	2.65	6
			2.94	6
Cadmium	3.06	8	2.97	6
			3.30	6
Gold	2.86	11	2.88	12

^a Data abstracted from Vineyard, 5

جدول ۱-۲: مقایسه خواص من جامد و مایع

خواص	جامد	مایع
وزن مخصوص در دمای ذوب (g/cm ³)	۸/۳۲	۷/۹۳
فاصله بین اتمی یا کمترین فاصله بین اتمها در دمای ذوب (Å)	۲/۷۴	۲/۸۸
ضریب تقارنت الکترونیکی در دمای ذوب (μΩ-cm)	۱۱	۲۲
ضریب نفوذ در دمای ذوب (cm ² /sec)	۱۰ ^{-۸}	۱۰ ^{-۵}
فاصله بین اتمی	مداول بریش	گرازیوی

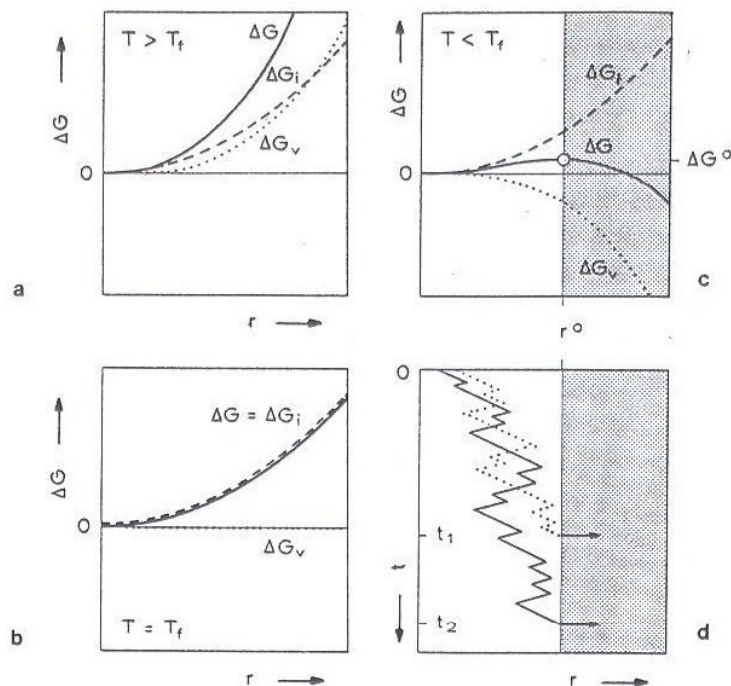


Figure 2.2 Free Energy of a Crystal Cluster as a Function of its Radius

The phenomenon of nucleation of a crystal from its melt depends mainly on two processes: thermal fluctuations which lead to the creation of variously sized crystal embryos (clusters), and creation of an interface between the liquid and the solid. The free energy change, ΔG_v , which is associated with the first process is proportional to the volume transformed. That is, it is proportional to the cube of the cluster radius. The free energy change, ΔG_i , which is associated with the second process is proportional to the area of solid/liquid interface formed. That is, it is proportional to the square of the cluster radius. At temperatures, T , greater than the melting point (a), both the volume free energy (ΔG_v) and the surface free energy (ΔG_i) increase monotonically with increasing radius, r . Therefore, the total free energy, ΔG , which is their sum, also increases monotonically. At the melting point (b), the value of ΔG_i still increases monotonically since it is only slightly temperature dependent. Because, by definition, thermodynamic equilibrium exists between the solid and liquid at the melting point, the value of ΔG_v is zero. Hence ΔG again increases monotonically with increasing radius. At a temperature below the equilibrium melting point (c), the sign of ΔG_v is reversed because the liquid is now metastable, while the behaviour of ΔG_i is still the same as in (a) and (b). However, ΔG_v has a 3rd-power dependence on the radius while ΔG_i has only a 2nd-power dependence. At small values of the radius, the absolute value of ΔG_v is less than that of ΔG_i , while at large values of r the cubic dependence of ΔG_v predominates. The value of ΔG therefore passes through a maximum at a critical radius, r^0 . Fluctuations may move the cluster backwards and forwards along the $\Delta G-r$ curve (c) due to the effect of random additions to, or removals of atoms from, the unstable nucleus (d). When a fluctuation causes the cluster to become larger than r^0 , growth will occur due to the resultant decrease in the total free energy. Thus, an embryo or cluster ($r < r^0$) becomes a nucleus ($r = r^0$) and eventually a grain ($r \gg r^0$).

Maximum undercoolings of melts

Material	Melting point (K)	Maximum † undercooling ΔT (C)		Material	Melting point (K)	Maximum undercooling ΔT (C)
		Large samples	Small †† samples			
Ag	1234		227	H ₂ O	273	39
Al	932		130	NH ₃	195.5	40
Au	1336		221	BF ₃	144.5	17.8
Bi	544	30	90	SO ₂	197.6	33
Co	1763		330	CH ₃ Cl	175.6	55.6
Cu	1356		236	CCl ₄	250	50.4
Ga	302.8	55	76	CBr ₄	363	82
Ge	1231	30	193	C ₆ H ₆	278	70
Fe	1803		295	(CH ₂ Br) ₂	282	66.5
Hg	234.1	14	46	C ₆ H ₅ COOH	395	120
Mn	1493		308	CH ₃ Br	179.4	24.4
Ni	1725		319	CH ₃ NH ₂	179.7	35.7
P	317	115	80	CHCl ₃	209.7	52.5
Pb	600.7		80	Diphenyl	344	86
Pd	1828		332	Naphthalene	353	94.4
Pr	2046		370	Cyclopropane	145.8	17.8
S	393	70	165	Thiophene	234.9	50.7
Sb	903		135	InSb	698	110
Se	493		25	InSb + 1% Te	690	55
Sn	505	31	115			

† Note that Burns and Turnbull (1966) have shown that the undercooling achieved depends on the rate of cooling.

†† The idea of using small samples is to reduce the chance of nucleation by a foreign solid particle. However, results on very small samples should be treated with care. Petrov (1965) has shown that samples of lead, bismuth and antimony with diameters of about 2.5×10^{-5} mm had melting points which differed from those found in the bulk by +53, -39 and -15 C respectively.

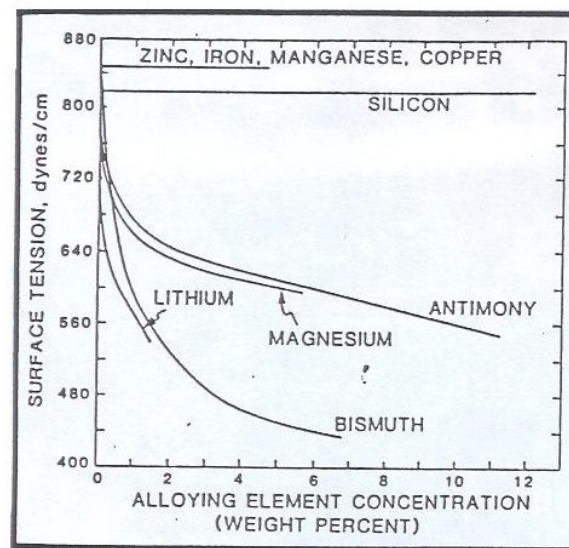


Figure 1. The Effect of Added Elements on the Surface Tension of Pure Aluminum at 700-740°C in Argon.

Type of melt	Range		Median
	$\Delta T/T$	γ_{LS} (erg cm ⁻²)	
Metals	0.13-0.32	32-260	130
Alkali halides	0.14-0.24	40-180	65
Molecular	0.12-0.32	7-35	24
Long chain hydrocarbons	0.037-0.043	7-10	9
Polymers	0.13-0.22		~20

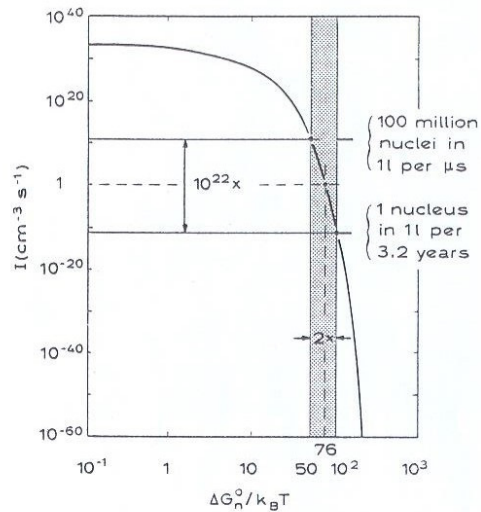


Figure 2.5 Nucleation Rate as a Function of Activation Energy, ΔG_n^0

Variations in the value of the term, $\Delta G_n^0/k_B T$, have a remarkable effect upon the rate of nucleation, I , due to the exponential relationship. If, for an observable rate of $I = 1/\text{cm}^3\text{s}$, $\Delta G_n^0/k_B T$ is changed by a factor of two, the resultant change in the nucleation rate is of the order of 10^{22} . Thus, changing the temperature or changing the value of ΔG_n^0 can enormously increase or decrease the nucleation rate. The value of ΔG_n^0 can be decreased by adding crystalline foreign particles which 'wet' the growing nucleus to the melt (inoculation), or by increasing the undercooling.

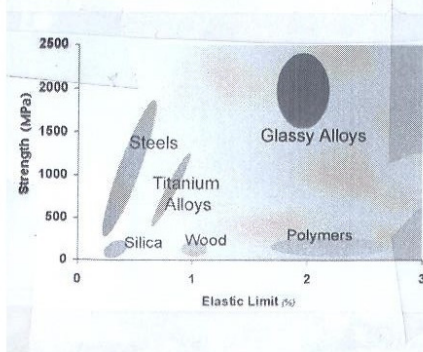


Figure 2.4 Nucleation Rate and Nucleation Time as a Function of Absolute Temperature

The overall nucleation rate, I (number of nuclei created per unit volume and time), is influenced both by the rate of cluster formation, which depends upon the nucleus concentration (N_n^0), and by the rate of atom transport to the nucleus. At low undercoolings, the energy barrier for nucleus formation is very high and the nucleation rate is very low. As the undercooling increases, the nucleus formation rate increases before again decreasing (a). The decrease in the overall nucleation rate, at large departures from the equilibrium melting point, is due to the decrease in the rate of atomic migration (diffusion) with decreasing temperature. A maximum in the nucleation rate, I_m , is the result. This information can be presented in the form of a TTT (time-temperature-transformation) diagram (b) which gives the time required for nucleation. This time is inversely proportional to the nucleation rate, and diagram (b) is therefore the inverse of diagram (a) for a given alloy volume. The diagram indicates that there is a minimum time for nucleation, t_m (proportional to $1/I_m$). This minimum value can be moved to higher temperatures and shorter times by decreasing the activation energy for nucleation, ΔG_n^0 [dash-dot line in (b)]. When liquid metals are cooled by normal means, the cooling curve will generally cross the nucleation curve (curve 1). However, very high rates of heat removal (curve 2) can cause the cooling curve to miss the nucleation curve completely and an amorphous solid (hatched region, glass) is then formed via a continuous increase in viscosity (Fig. 1.1). Note that this figure relates to nucleation (start of transformation) only. The second curve of a TTT diagram which describes the end of the transformation, after growth has occurred, is not shown.

Table 2.1 Critical Dimensions and Activation Energy for the Nucleation of a Spherical Nucleus in a Pure Melt ($\Delta g = \Delta s_f \Delta T$)

	Homogeneous Nucleation	Heterogeneous Nucleation
r^0	$-\frac{2\sigma}{\Delta g}$	$-\frac{2\sigma}{\Delta g}$
n^0	$-\left(\frac{32\pi}{3v^*}\right)\left(\frac{\sigma}{\Delta g}\right)^3$	$-\left(\frac{32\pi}{3v^*}\right)\left(\frac{\sigma}{\Delta g}\right)^3 f(\theta)$
ΔG_n^0	$\left(\frac{16\pi}{3}\right)\left(\frac{\sigma^3}{\Delta g^2}\right)$	$\left(\frac{16\pi}{3}\right)\left(\frac{\sigma^3}{\Delta g^2}\right) f(\theta)$

Table 2.2 Values of the Expression: $f(\theta) = (1/A)(2 + \cos\theta)(1 - \cos\theta)^2$

θ ($^\circ$)	Type of Nucleation (no nucleation barrier #)	$f(\theta)$
0 complete wetting	0	0.00017
10	heterogeneous	0.0027
20		0.013
30		0.038
40		0.084
50		0.25 *
70		0.5
90		0.75
110		0.92
130		0.99
150		0.99998
170	homogeneous	1
180 no wetting		

*#) immediate growth can occur

TABLE 2.2
COMPOUNDS USED TO STUDY THE HETEROGENEOUS NUCLEATION
OF ALUMINUM FROM ITS MELT*

Compound	<i>C</i> crystal structure	<i>d</i> for close-packed planes	Nucleating effect
VC	Cubic	0.014	Strong
TiC	Cubic	0.060	Strong
TiB ₂	Hexagonal	0.048	Strong
AlB ₂	Hexagonal	0.038	Strong
ZrC	Cubic	0.145	Strong
NbC	Cubic	0.086	Strong
W ₂ C	Hexagonal	0.035	Strong
Cr ₃ C ₂	Complex	---	Weak or nil
Mn ₃ C	Complex	---	Weak or nil
Fe ₃ C	Complex	---	Weak or nil

TABLE 6.1
SOME GRAIN REFINING NUCLEANTS*

Metal or alloy	Grain refiner	Comments
Magnesium and Mg-Zr alloys	Zirconium added as alloy or salts	Zr or Zr-enriched Mg peritectic nuclei
Magnesium-aluminum alloys	Carbon, for example as hexachlorethane	Al ₄ C ₃ or Al ₁₃ Mg ₄ C ₃ nuclei
Magnesium-aluminum alloys	Superheating	In presence of C, Al ₄ C ₃ and/or Al-Mn nuclei
Magnesium-aluminum-manganese	FeCl ₃	Fe-Al-Mn or Al ₄ C ₃ nuclei
Mg-Zn	FeCl ₃ or Zn-Fe NH ₃	Fe compound nuclei
Al alloys	Ti as reducible halide salts or as Al-Ti hardener	Nucleated by H ₂ (?)
Al alloys	Ti + B as reducible halide salts or as Al-Ti-B hardener	TiC nucleus or peritectic TiAl ₃
Al alloys	Boron as reducible halide salts or Al-B	TiB ₂ nuclei, more resistant to melt history
Al alloys	Niobium	Fe-rich peritectic nuclei
Cu alloys	Fe metal or alloy	
Bronzes	Transition nitrides and borides or FeB	
Cu-Al ₂ Cu eutectic	Titanium	Nucleates primary Al
Cu-7%Al	Mo, Nb, W, V	
Cu-9%Al	Bi	
Low alloy steel	Titanium	
Low alloy steel	Transition elements and carbides	
Silicon steel	TiB ₂	
Low alloy steel	Fe powder	Dissolves and precipitates TiN or TiC
Austenitic steel	CaCN ₂ , nitrided Cr and other metallic powders	Introduction of micro-chilling particles
Tin alloys	Germanium or indium	In presence of increased nitrogen
Lead alloys	S	
Lead alloys	Se, Te	
Type metal	As, Te	
Monel	Lithium	
Al-Si hypereutectic	Phosphorus as Cu-P, PNCl ₃ or proprietary inoculant	Refines primary Si
Fe-C (graphite)	Carbon	Refines eutectic, probably through nucleating graphite
Fe-C-Si (graphite)		
Grey cast iron	Si alloys containing aluminum, alkaline earths and/or rare earths	Refines eutectic, may nucleate through precipitation of carbides or graphite

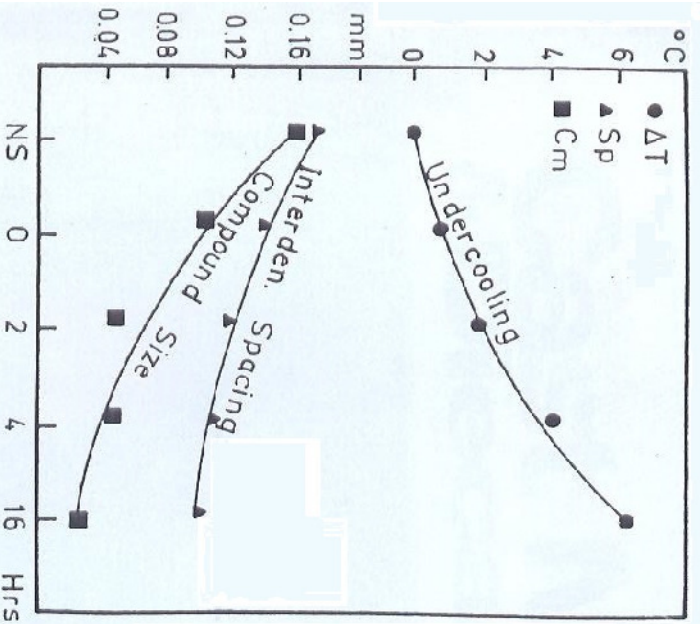


Fig. 25: b) Effect of superheating and holding at high temperature on undercooling, interdendritic spacing and size of intermetallic compound. NS = not superheated, 0 = Superheated 450°C and cooled immediately to pouring temperature; 2, 4, 16 = held at superheating temperature for 2, 4, 16 hours respectively before cooling to pouring temperature.

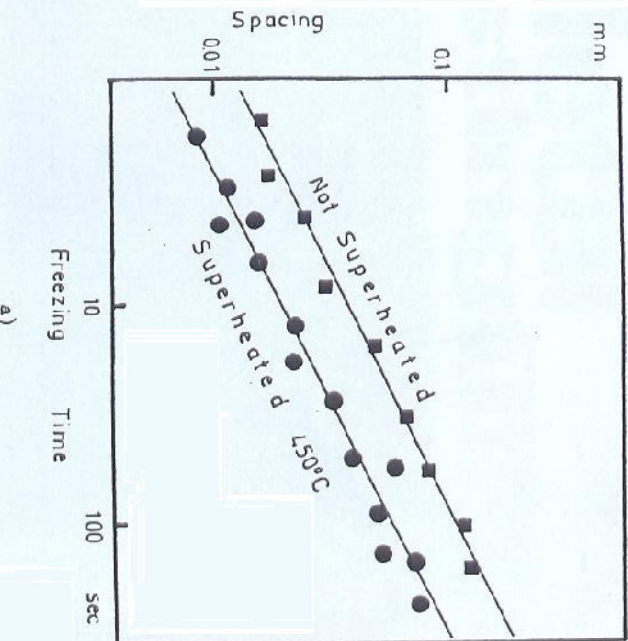


Fig. 25: a) Effect of superheat on interdendritic spacing and structure.
a) Effect of superheating on growth of spacing during solidification.

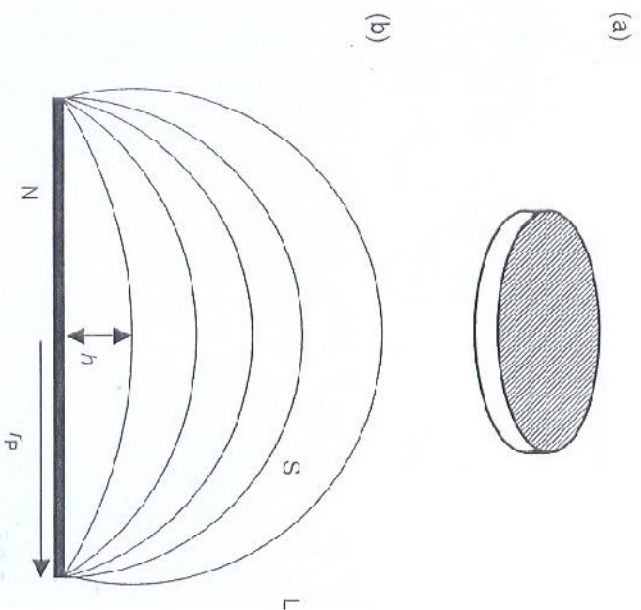


Figure 1. Hexagonal TiB_2 particles in Al-Ti-B master alloys can be approximated as circular discs (a). Nucleation of $\alpha\text{-Al}$ occurs on the circular $\{0001\}$ faces only. Growth (b) of the nucleated solid S into the liquid L and outward from the face of the particle N involves an increase in curvature of the liquid/solid interface as permitted by an increase in undercooling. The curvature is maximum when the liquid/solid interface is hemispherical. Free growth beyond that point during cooling constitutes athermal nucleation.

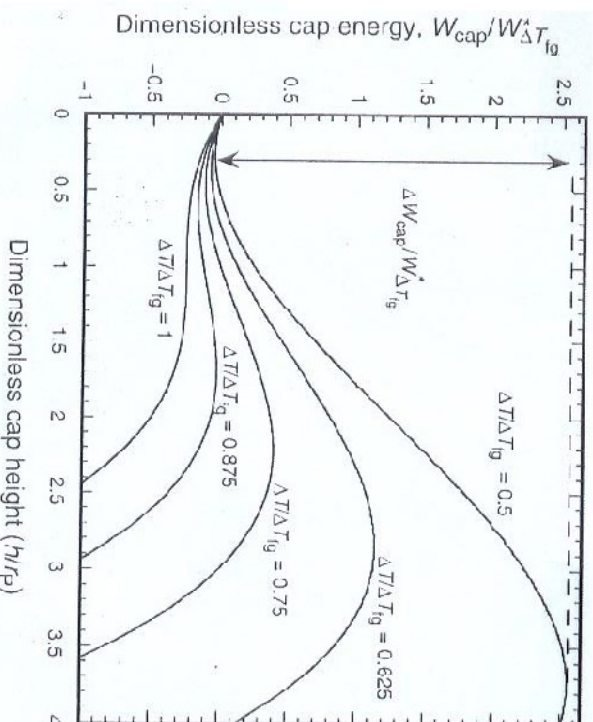


Figure 2. Dimensionless work of formation ($W_{\text{cap}}/W_{\Delta T_{fg}}^*$) of solid cap on a circular nucleant area as a function of dimensionless cap height (h/r_p) for selected values of dimensionless undercooling ($\Delta T/\Delta T_{fg}$) (equation (5)). The minima (maxima) in these energy curves represent metastable (unstable) equilibrium configurations.

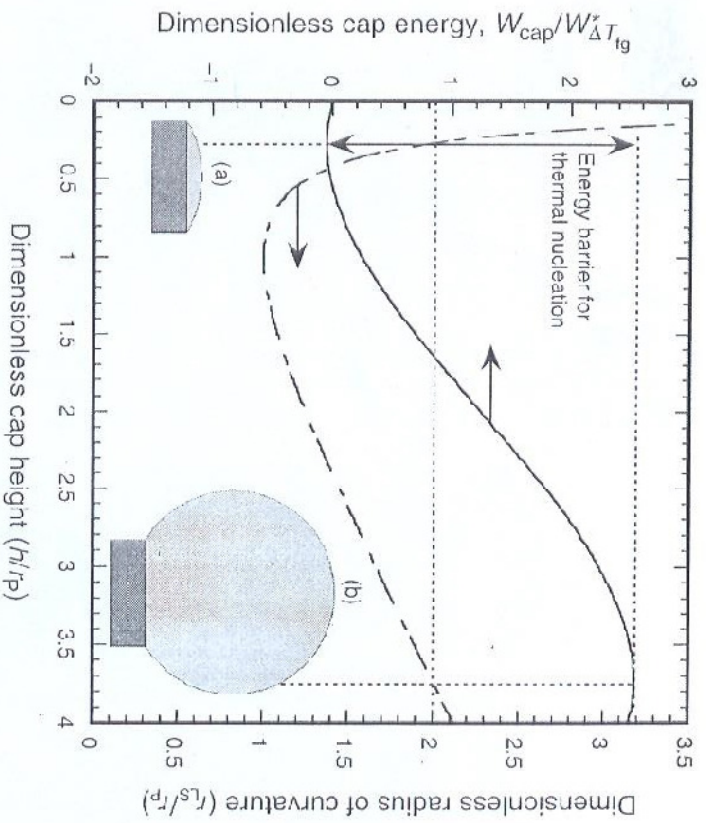


Figure 3. The dimensionless work of formation ($W_{cap}^*/W_{\Delta T_{fg}}^*$) of the solid cap and the radius of curvature of the liquid/solid interface (r_{ls}/r_p) as a function of the dimensionless cap height (h/r_p) at a dimensionless undercooling of 0.5. The barrier for nucleation is the energy difference between the extrema on the work curve. The inset diagrams illustrate (a) the metastable equilibrium and (b) the unstable equilibrium configurations of solid (light-grey shading) for a dimensionless undercooling of 0.5.

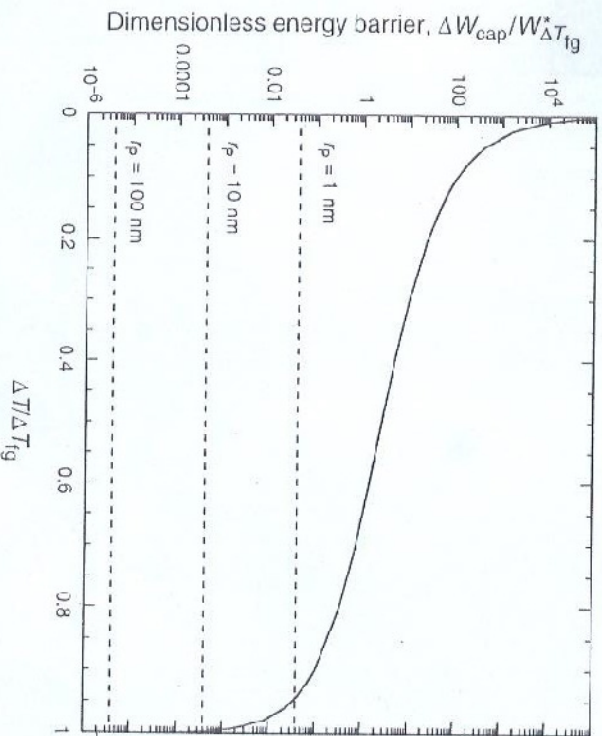
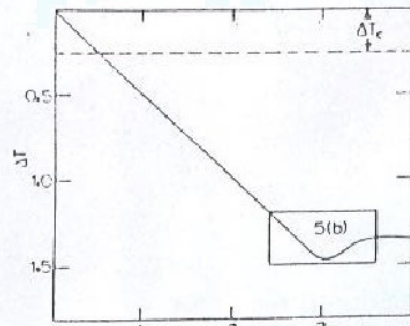
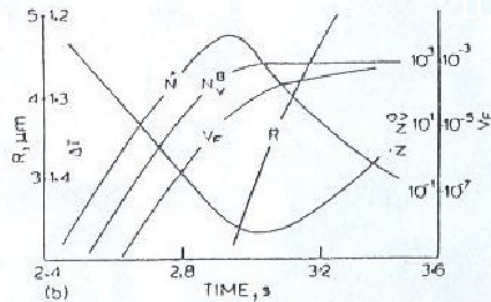


Figure 4. The dimensionless critical work of nucleation ($\Delta W_{cap}^*/W_{\Delta T_{fg}}^*$) as a function of dimensionless undercooling ($\Delta T/\Delta T_{fg}$) (equation (7)) for a solid cap forming on a circular nucleant area. The dashed lines indicate values (dependent on particle radius r_p) of the critical work below which, during cooling, thermal activation of nucleation is likely to precede the onset of free growth (equation (8)). Calculations are for aluminum alloys.

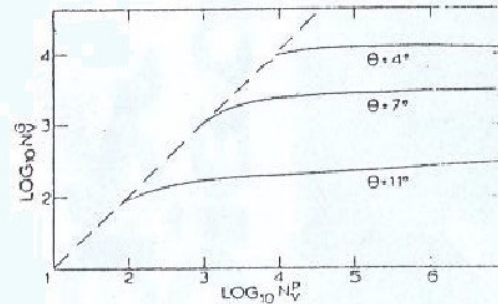


(a)

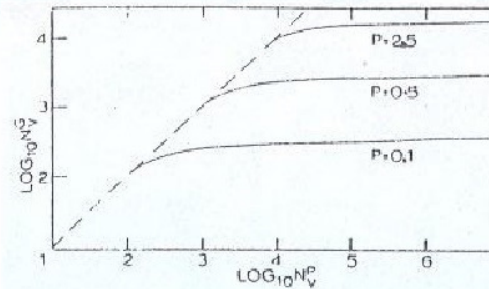


(b)

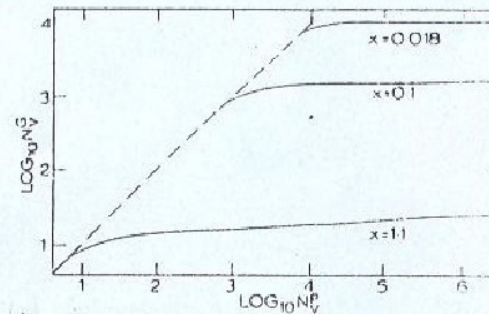
5 *a* Cooling curve computed for Al-Ti alloy containing 10^3 mm^{-3} particles of Al_3Ti , radius $R_0 = 1 \mu\text{m}$, initial cooling rate 0.5 K/s and $\theta = 7^\circ$; *b* detail taken from inset Fig. 5*a* showing corresponding variations of \dot{N} = number of nucleation events mm^{-3}/s , N_v^0 = total number of nucleation events mm^{-3} , V_F = volume fraction of solid metal, and R = mean radii of solid metal spheres



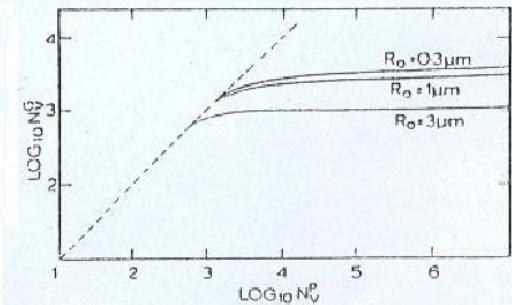
6 Plotting number of grains mm^{-3} v. number of particles mm^{-3} for Al-Ti system, Al_3Ti radius $1 \mu\text{m}$ and cooling rate 0.5 K/s ; for three values of the hypothetical contact angle $\theta = 4^\circ$, $\theta = 7^\circ$, and $\theta = 11^\circ$



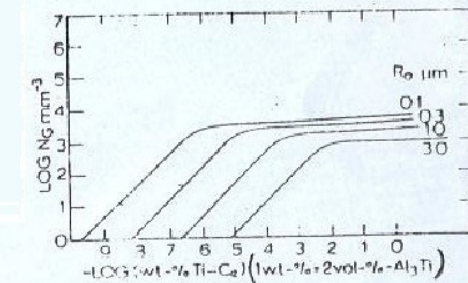
7 As Fig. 6 with $\theta = 7^\circ$ and for cooling rates $P = 0.1 \text{ K/s}$, $P = 0.5 \text{ K/s}$ and $P = 2.5 \text{ K/s}$



8 As Figs 6-7, with $\theta = 4^\circ$, $P = 0.5 \text{ K/s}$, and for phase diagram data, X , from AlTi ($X = 0.018$), Al-Zr ($X = 0.1$) and Al-Cr ($X = 1.1$), where $X = \frac{1}{2}(C_0 m (k-1))$



9 As Figs 6-8, with $\theta = 7^\circ$, $P = 0.5 \text{ K/s}$ for $X = 0.018$ (AlTi) and particle radii, $R_0 = 3 \mu\text{m}$, $1 \mu\text{m}$ and $0.3 \mu\text{m}$.



11 Data from Fig. 9 replotted for different particle sizes as functions of excess Ti concentration beyond the effective liquidus concentration C_e .

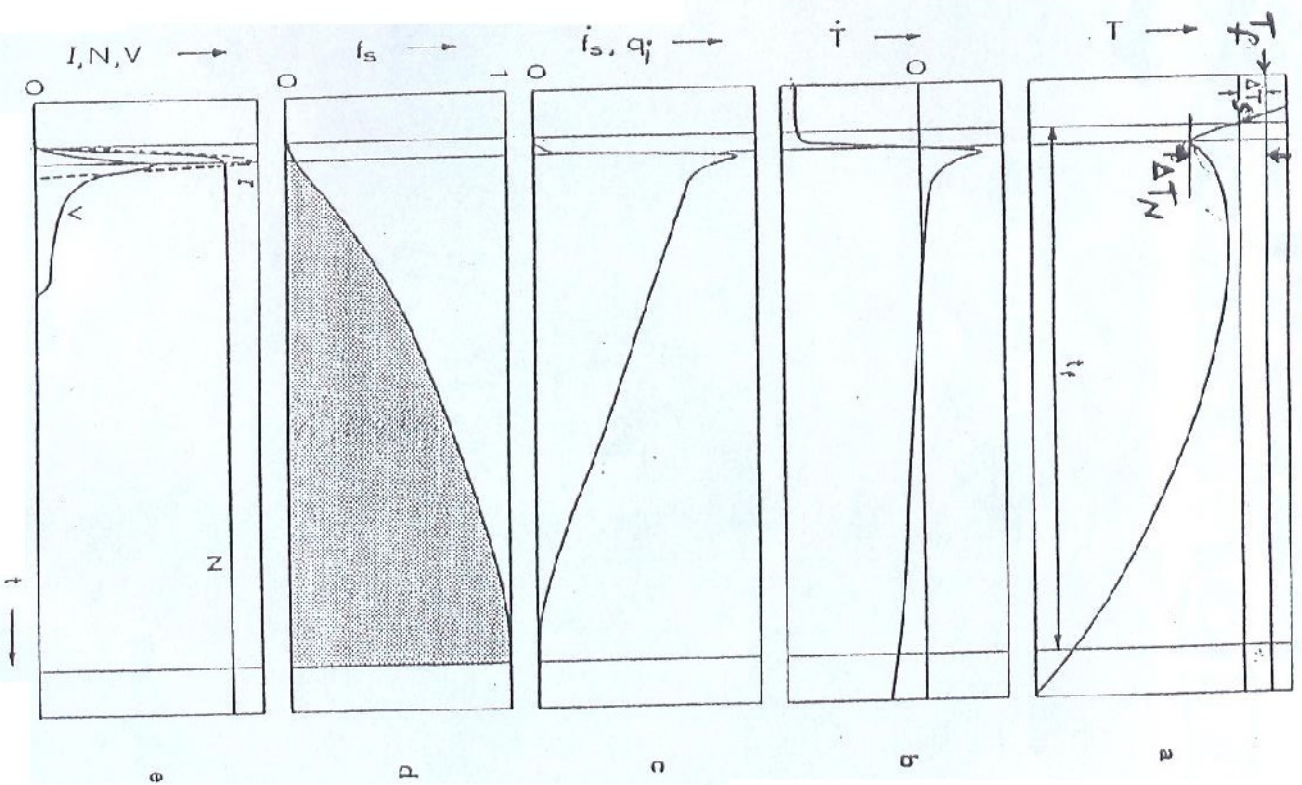


Figure 2.1 Thermal History of Equiaxed Dendritic Solidification

The above temperature-time curve is one which might well be obtained during a solidification sequence such as that pictured in figure 1.9a. The usual cooling curve (a) begins to deviate slightly at the undercooling where nucleation occurs, ΔT_N . At this point, the first fraction of solid, f_s , appears (d). With further cooling, the nucleation rate, I , rapidly increases to a maximum value (e). At the minimum in the temperature-time curve, the growth rate, V , of the grains (i.e. of the dendrite tips) is at its highest. The subsequent increase in temperature is due to the high internal heat flux, q_f , arising from the rate of transformation, $f_s (= df_s/dt)$, and the latent heat released (c). (The maximum of the temperature can lie above the nucleation temperature.) Note that I is much more sensitive to temperature changes than is V (e). Most of the solidification which takes place after impingement of the grains involves dendrite arm coarsening at a dip growth rate, V , equal to zero. During this time interval, the number of grains, N , remains constant.

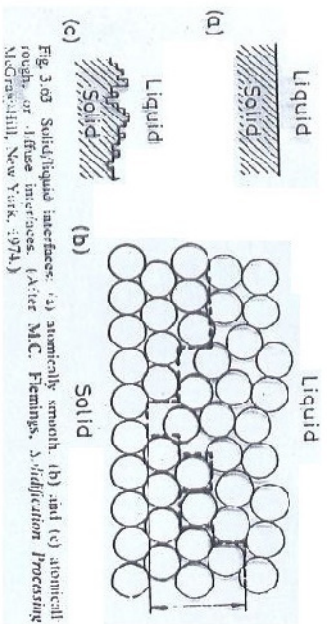


Fig. 3.03 Solid/liquid interfaces: (a) atomically smooth, (b) and (c) atomically rough, or diffuse interfaces. (After M.C. Flemings, *Diffusion Processing* McGraw-Hill, New York, 1974.)

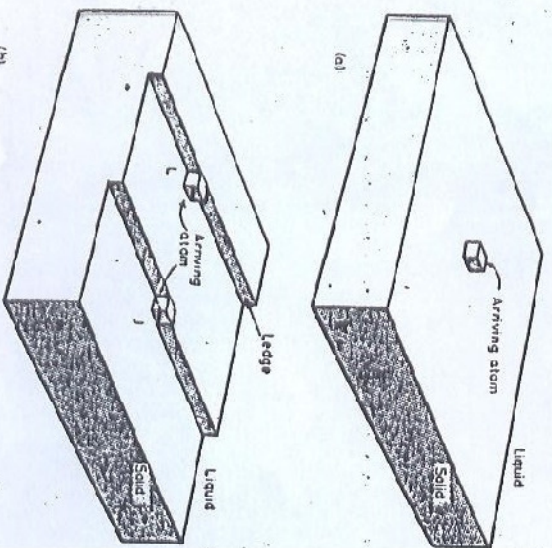


Fig. 4.11 Atomically smooth solid/liquid interfaces with atoms represented by cubes: (a) Addition of a single atom onto a flat interface increases the number of broken bonds by four. (b) Addition to a ledge (L) only increases the number of broken bonds by two, whereas at a jog in a ledge (J) there is no increase.

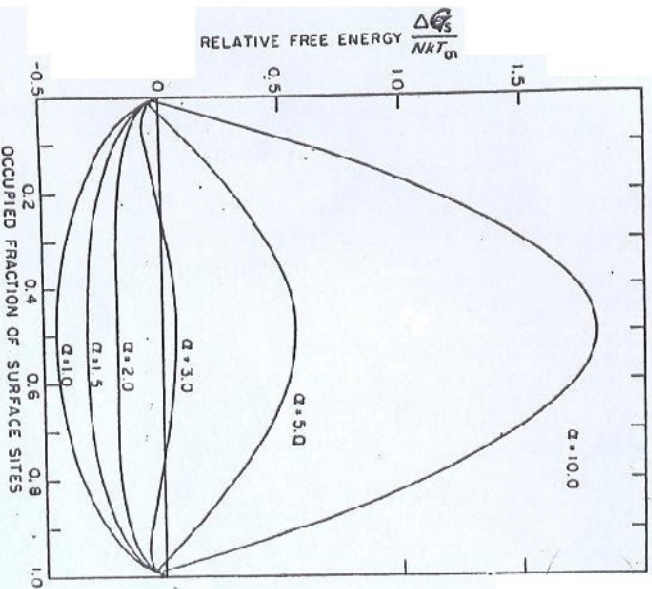


Fig. 3.1 Relative change in surface free energy as a function of the fraction of surface sites which are occupied. α depends on the crystal face, the type of crystal and the phase from which the crystal is growing (Jackson¹).

Table 2.4 Growth Morphologies and Crystallisation Entropies

Dimensionless Entropy ($\Delta S_f/R$)	Superaturated Substance	Phase	Morphology
~1	metals	melt	non-faceted
~1	'plastic' crystals	melt	non-faceted
2-3	semiconductors	solution	n/faceted
2-3	semimetals	solution	n/faceted
~6	molecular crystals	solution	faceted
~10	metals	vapour	faceted
~20	complex molecules	melt	faceted
~100	polymers	melt	faceted

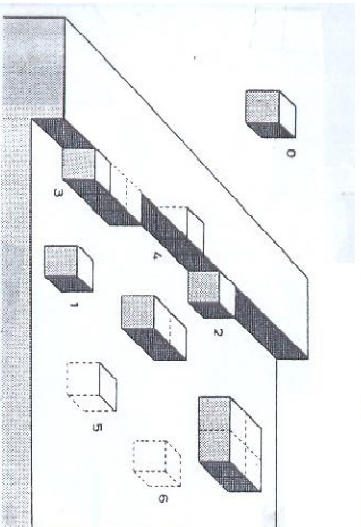


Figure 2.7 Variation in Bond Number at the Solid/Liquid Interface of a Simple-Cubic Crystal

In order to understand the two types of growth shown in figure 2.6, the various ways in which an atom can be adsorbed at the solid/liquid interface have to be considered. Growth is determined by the probability that an atom will reach the interface and remain adsorbed there until it has been fully incorporated into the crystal. This probability increases with an increasing number of nearest neighbours in the crystal. The possible arrangements of atoms on the crystal interface are indicated here, where the numbers specify the number of neighbouring atoms in the crystal (when the coordination number is 6 as in a simple cubic crystal). The atoms of the liquid phase are not shown here. A special role is played by type 3 atoms in the growth of faceted crystals because, having three bonds, they can be considered to be situated half in the solid and half in the liquid. A likely growth sequence would be: addition of type 3 atoms until a row is complete; addition of a type 2 atom to start a new row; and so on until a layer is complete. Thereupon, nucleation of a new layer by the addition of a type 1 atom would be necessary. This is an unfavourable process and requires a very high undercooling. Therefore, other processes will play a role (fig. 2.10).

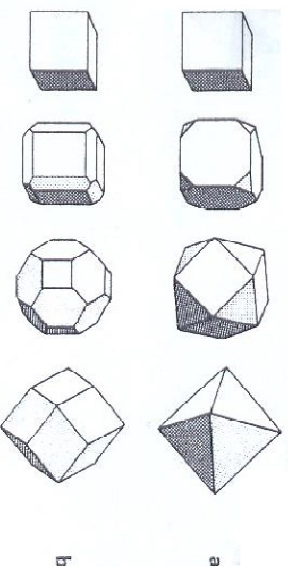


Figure 2.9 Development of Faceted Crystal Growth Morphologies

A growing cubic crystal which is originally bounded only by (100) planes (left hand side) will change its shape to an octahedral form (bounded by {111}) when the (100) planes grow more quickly than the {111} planes (a). Often, impurities change the growth behaviour of specific planes and this results in the appearance of different growth forms for the same crystal structure. Here the {110} planes are the slowest growing, this will lead to a rhombicuboctahedron (b). The slowest growing planes (usually of low index type) always dictate the growth habit of the crystal. The resultant minimum growth rate form is not the same as the equilibrium (non-growing) form, which is governed by minimisation of the total surface energy.

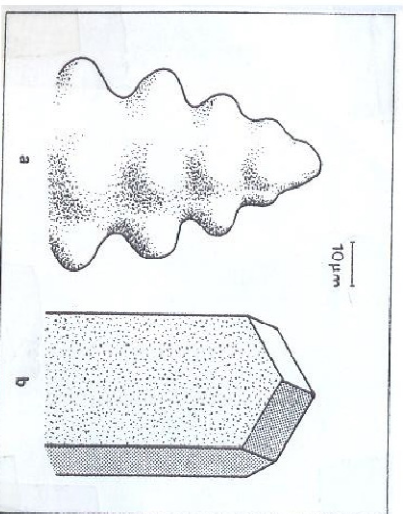


Figure 2.6 Non-Faceted and Faceted Growth Morphologies

After nucleation has occurred, further atoms must be added to the crystal in order that growth can continue. During this process, the solid/liquid interface takes on a specific structure at the atomic scale. Its nature depends upon the differences in structure and bonding between liquid and solid. During the solidification of a non-faceted material, such as a metal (a), atoms can be added easily to any point of the surface and the crystal shape is dictated mainly by the interplay of capillary effects and diffusion (of heat and/or solute). Nevertheless, a remaining slight anisotropy in properties such as the interface energy leads to the growth of dendritic arms in specific crystallographic directions. In faceted materials, such as inorganic salts or minerals (b), the inherently rough, high index planes accept added atoms readily and grow quickly. As a result, these planes disappear and the crystal remains bounded by the more slowly growing facets (low index planes). The classes of non-faceted and faceted crystals can be distinguished on the basis of the higher entropy of fusion of the latter. This is due to the greater difference in structure and bonding between the solid and liquid phases as compared to metals, which exhibit only very small differences between the two phases.

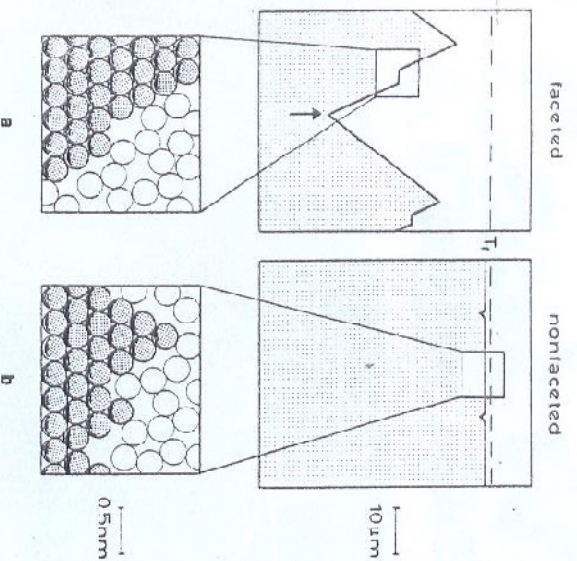


Figure 2.8 Form of Faceted (a) and Non-Faceted (b) Interfaces
 A transparent organic substance, when observed under the microscope during directional solidification (upwards growth, bottom cool, top hot), can exhibit either a faceted interface (a) or jagged and faceted air diagrams. It is important to note that during growth a faceted interface (a) is jagged and faceted at microscopic scale (upper diagram), but smooth at the atomic scale (lower diagram). On the other hand, non-faceted interface (b) can be microscopically flat with some slight depressions due to grain boundaries (upper diagram), while at the atomic scale it is rough and uneven (lower diagram). The roughness causes the attachment of atoms to be easy and largely independent of the crystal orientation. Note also that the interface of a non-faceted material will grow at a temperature which is close to the melting point, T_f , while the interface of a faceted material might have a very high local undercooling (such a point (arrow) is a re-entrant corner (Fig. 2.10), and is associated with an increased number of nearest neighbours. Thus, growth will tend to spread from here.

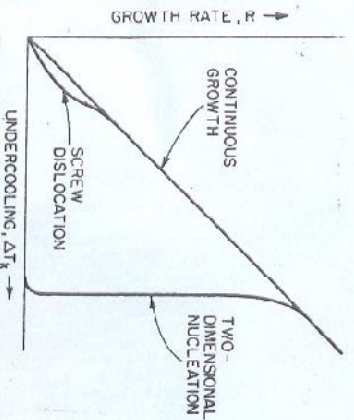


FIGURE 9-14 Growth rate versus interface undercooling according to the three classical laws

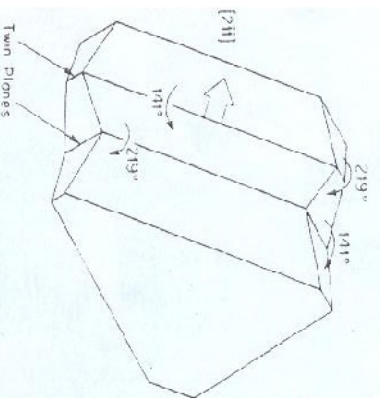


FIGURE 9-24 Gemantium crystal with two twin planes has six favored reentrant sites 60° apart (From Hamilton and Seidenstricker '47)

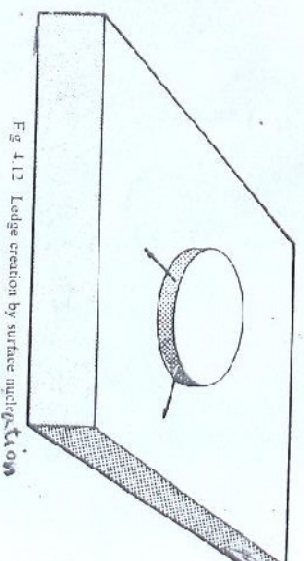


Fig. 4.13 Ledge creation by surface multiplication

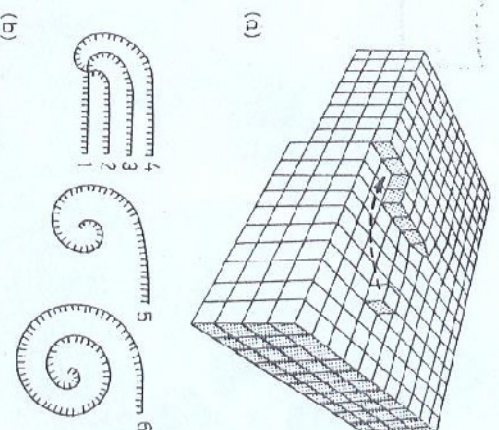


Fig. 4.13 Spiral growth. (a) A screw dislocation terminating in the solid/liquid interface causing the associated ledge. (After W.T. Reilly, *Dislocations in Crystals*, © 1955 McGraw-Hill. Used with the permission of McGraw-Hill Book Company.) Addition of atoms at the ledge causes it to rotate with an angular velocity decreasing away from the dislocation core so that a growth spiral develops as shown in (b). (After J.W. Christian, *The Theory of Phase Transformations in Metals and Alloys*, Pergamon Press, Oxford, 1965.)

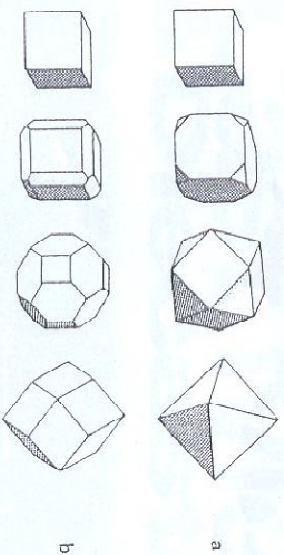


Figure 2.9. Development of faceted crystal growth morphologies

A growing cubic crystal which is originally bounded only by (100) planes (left hand side) will change its shape to an octahedral form (bounded by (111)) when the (100) planes grow more quickly than the (111) planes (a). Often, impurities change the growth behaviour of specific planes and this results in the appearance of different growth forms for the same crystal structure. If the (110) planes are the slowest growing, this will lead to a rhombicuboctahedral dodecahedron (b). The slowest growing planes (usually of low-index type) always dictate the growth habit of the crystal. The resultant minimum growth rate form is not the same as the equilibrium (fast growing) form, which is governed by minimisation of the total surface energy.

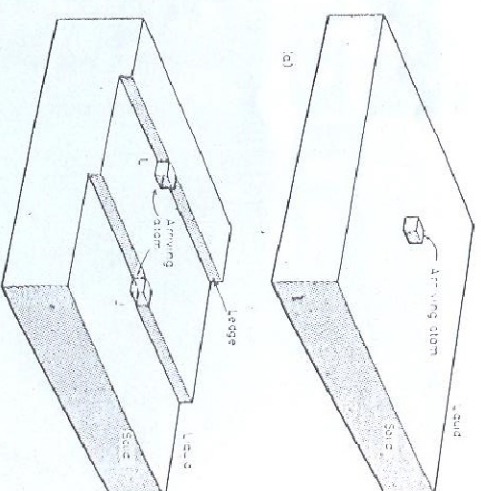


Fig. 4.11. Achemically smooth solid-liquid interfaces with atoms, represented by cubes. (a) Addition of a single atom onto a flat interface increases the number of broken bonds by four. (b) Addition to a ledge (L) only increases the number of broken bonds by two, whereas at a jog in a ledge (J) there is no increase.

Table 2.4 Growth Morphologies and Crystallisation Entropies

Dimensionless Entropy ($\Delta S^*/R$)	Supersaturated Substance	Phase	Morphology
-1	metals	melt	non-faceted
-1	plastic crystals	melt	non-faceted
2-3	semiconductors	solution	s/faceted
2-3	semimetals	solution	s/faceted
-6	molecular crystals	solution	faceted
-10	metals	vapour	faceted
-20	complex molecules	melt	faceted
-100	polymers	melt	faceted

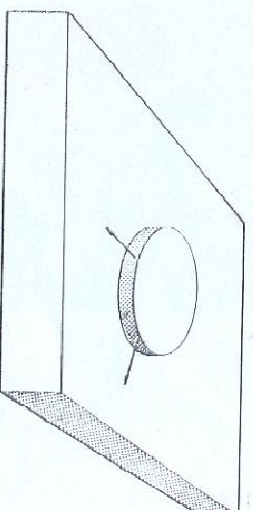


Fig. 4.12. Ledge creation by surface energy. (C. O. S.)

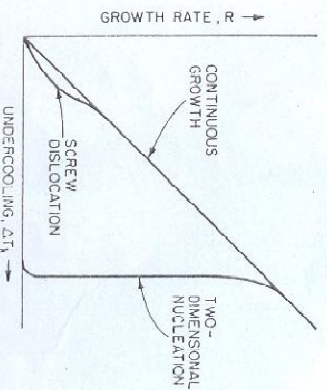


FIGURE 9-14 Growth rate versus interface undercooling according to the three classical laws.

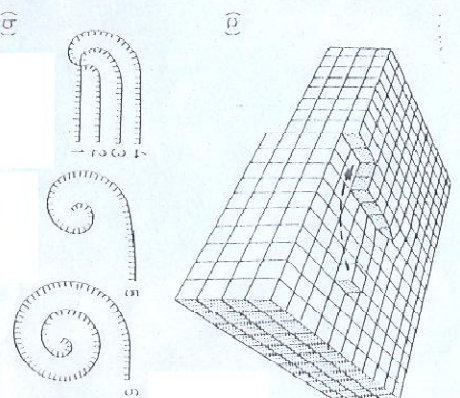


Fig. 4.13. Spiral growth. (a) A screw dislocation terminating in the solid-liquid interface, showing the associated ledge. (After W. T. Read, Jr., *Dislocations in Crystals*, © 1953 McGraw-Hill, Inc.) (b) In the presence of MgO dust (Hill, Book Company), a number of spirals of the above nature, it is possible to find regular helical structures away from the dislocation sites so that a growth spiral develops as shown in (b). (After J. V. Christian, *The Theory of Phase Transformation in Metals and Alloys*, Pergamon Press, Oxford, 1965.)

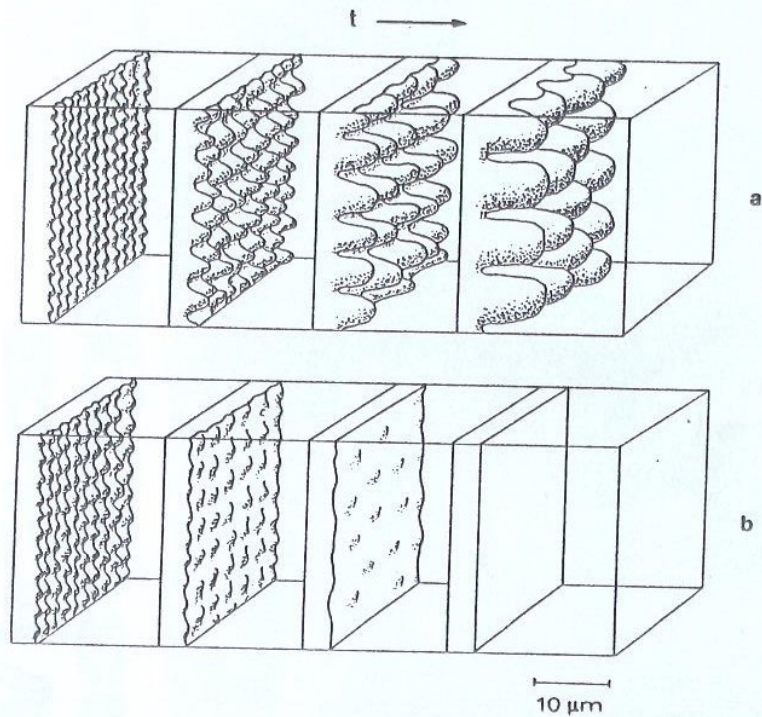


Figure 3.1 Initial Evolution of an Unstable (a) or Stable (b) Interface

Such an interface might be seen during the microscopic observation of transparent non-faceted organic substances. During growth, any interface will be subject to random disturbances caused by insoluble particles, temperature fluctuations, or grain boundaries. A stable interface is distinguished from an unstable interface by its response to such disturbances. It is imagined here that the interface is initially slightly distorted by a spatially regular disturbance. If the distorted interface is unstable (a), the projections may find themselves in a more advantageous situation for growth and therefore increase in prominence. In the case of a stable interface (b), the perturbations will be unfavourably situated and tend to disappear. During the casting of alloys, the solid/liquid interface is usually unstable. A stable interface is only obtained in special cases such as columnar solidification of pure metals (Fig. 1.7a) or directional solidification of alloys in a Bridgman-type furnace (Fig. 1.4a) under a sufficiently high temperature gradient, G . The indicated scale is typical for alloys under normal casting conditions.

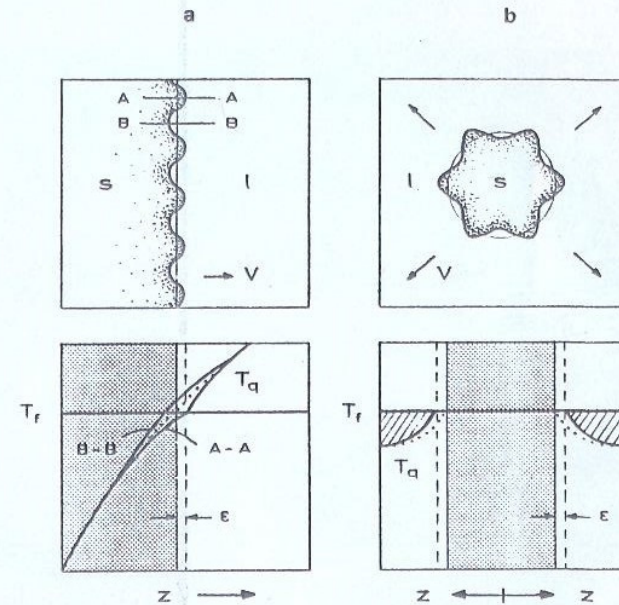


Figure 3.2 Columnar and Equiaxed Solidification of a Pure Substance

In a pure substance, stability depends on the direction of heat flow. In directional solidification, as in the columnar zone of a casting, the liquid temperature always increases ahead of the interface (a). Therefore, the heat flow direction is opposite to that of solidification. When a perturbation of amplitude, ϵ , forms at an initially smooth interface, the temperature gradient in the liquid increases while the gradient in the solid decreases (compare full and dotted lines along section, A-A). Since the heat flux is proportional to the gradient, more heat then flows into the tip of the perturbation and less flows out of it into the solid. As a result, the perturbation melts back and the planar interface is stabilised. In equiaxed solidification, the opposite situation is found (b). Here, the free crystals grow into an undercooled melt (cross-hatched region) and the latent heat produced during growth also flows down the negative temperature gradient in the liquid. A perturbation which forms on the sphere will make this gradient steeper (full line compared to the dotted line) and permit the tip to reject more heat. As a result, the local growth rate is increased and the interface is always morphologically unstable.

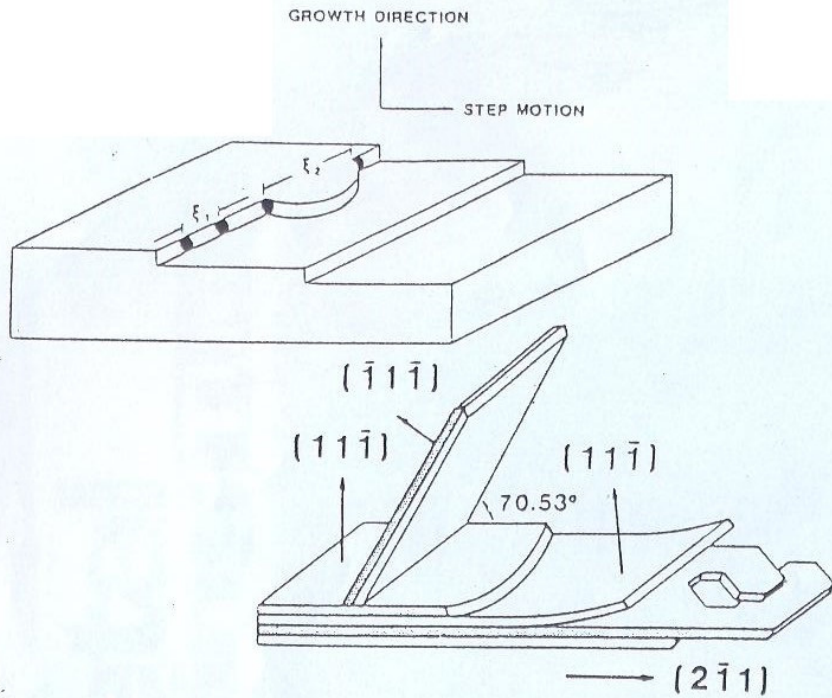


Figure 6: Adsorption of impurity atoms on growth steps of a silicon crystal causes twinning to occur. (After reference 2)

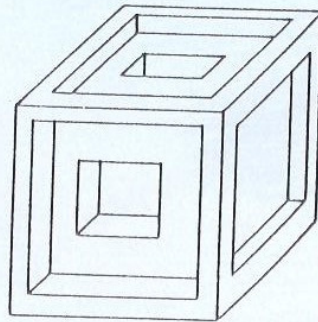


FIGURE 9-32
Idealized representation of development of hopper crystals.

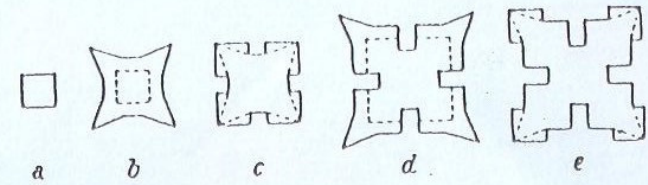


FIGURE 9-28
Development of a KCl dendrite. (From Papapetrou.⁵⁴)

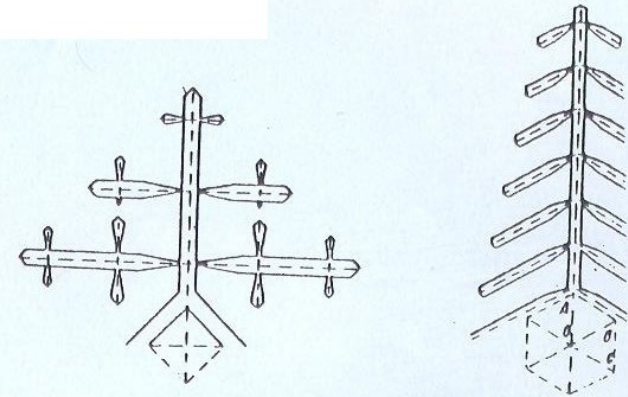


FIGURE 9-30
Faceted dendrites of materials of two different crystal structures. (I Saratovkin.⁵⁵)

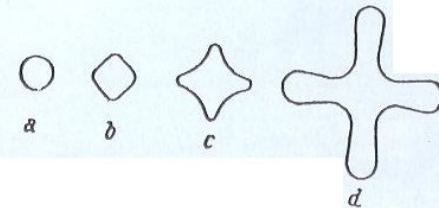


FIGURE 9-29
Development of a NH_4Cl dendrite. (From Papapetrou.⁵⁴)

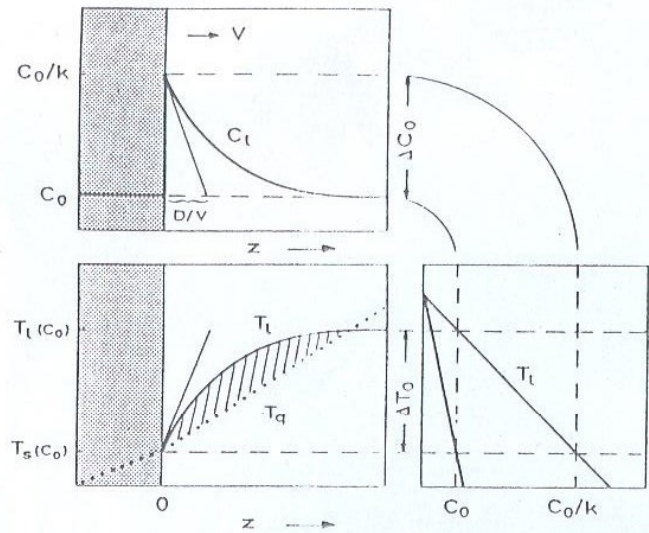


Figure 3.4 Constitutional Undercooling in Alloys

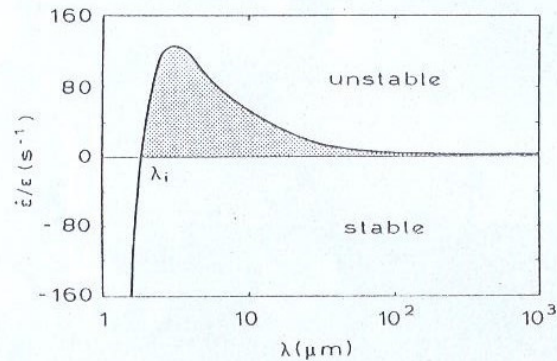


Figure 3.7 Rate of Development of a Perturbation at a Constitutionally Undercooled Interface

Here the parameter, $\dot{\epsilon}/\epsilon$, describes the relative rate of development of the amplitude of a small sinusoidal perturbation in the case of a specific alloy (Al-2wt%Cu) under given growth conditions ($V = 0.1\text{mm/s}$, $G = 10\text{K/mm}$). At very short wavelengths, the value of this parameter is negative due to curvature damping and the perturbation will tend to disappear (Fig. 3.1b). At wavelengths greater than λ_i and above, the sinusoidal shape will become more accentuated (instability - figure 3.1a). The wavelength having the highest rate of development is likely to become dominant. The reason for the tendency to stability at high λ -values is the difficulty of diffusional mass transfer over large distances. When the interface is completely stable, the curve will remain below the $\dot{\epsilon}/\epsilon = 0$ line for all wavelengths. This implies the disappearance of perturbations having any of these wavelengths (appendix 7).

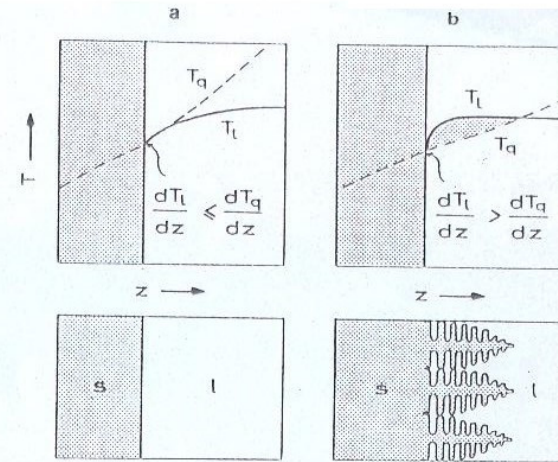


Figure 3.5 Condition for Constitutional Undercooling at the Solid/Liquid Interface, and the Resultant Structures

When the temperature gradient due to the heat flux is greater than the liquidus temperature gradient at the solid/liquid interface, the latter is stable (a). On the other hand, it can be seen that a driving force for interface change will be present whenever the slope of the local melting point curve (liquidus temperature) at the interface is greater than the slope of the actual temperature distribution. This is easily understood since the undercooling encountered by the tip of a perturbation advancing into the melt increases and therefore a planar interface is unstable (b). Note that the temperature profile in (b) is only hypothetical; after the dendritic microstructure shown in the lower figure has developed, the region of constitutional undercooling is largely eliminated. Only a much smaller undercooling remains at the tips of the dendrites as is shown in figure 4.7c.

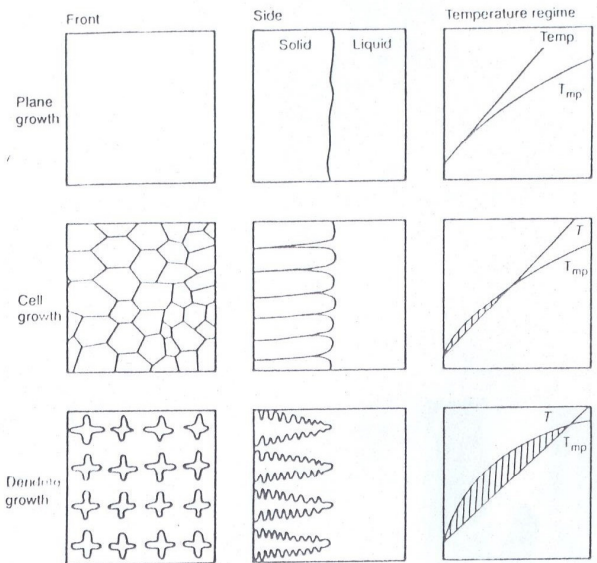


Figure 4.20 The transition of growth morphology from planar, to cellular, to dendritic, as compositionally induced undercooling increases (equivalent to G/R being reduced).

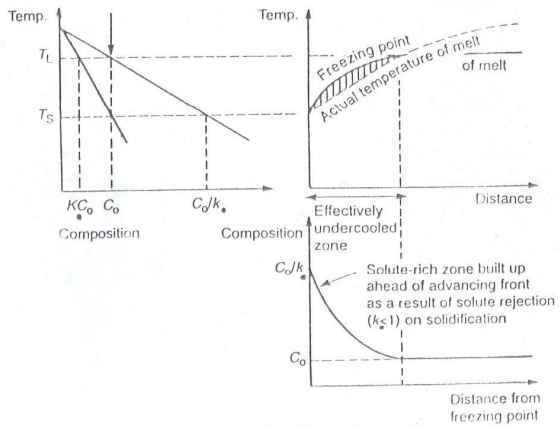


Figure 4.21 The link between the constitutional phase diagram for a binary alloy, and constitutional undercooling on freezing.

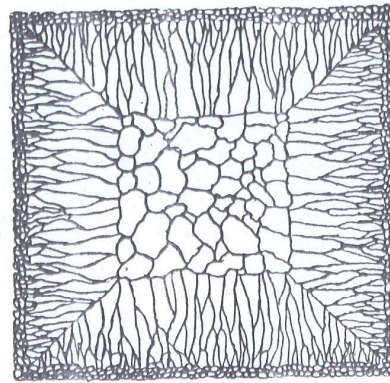


FIGURE 5-1 Sketch of ingot structure showing chill zone, columnar zone, equiaxed zone. (From Bower and Flemings.¹)

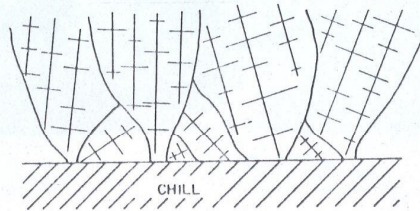


FIGURE 5-25 Development of a preferred texture at a chill face.

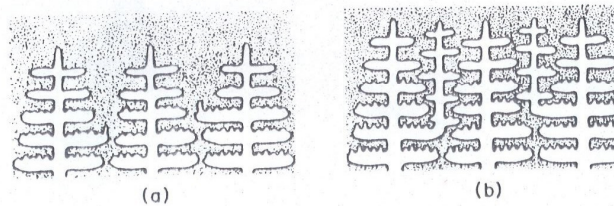


FIGURE 5-14 Formation of new primary arms by branching from secondaries.

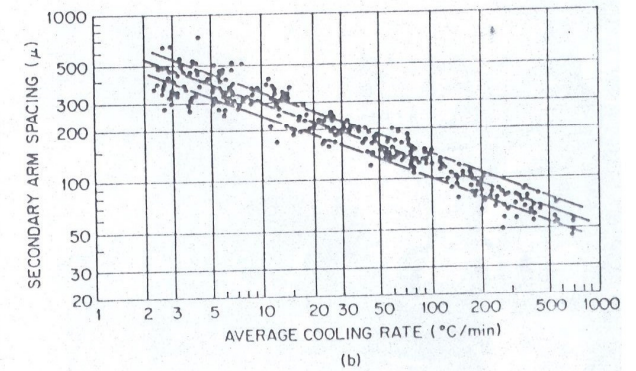
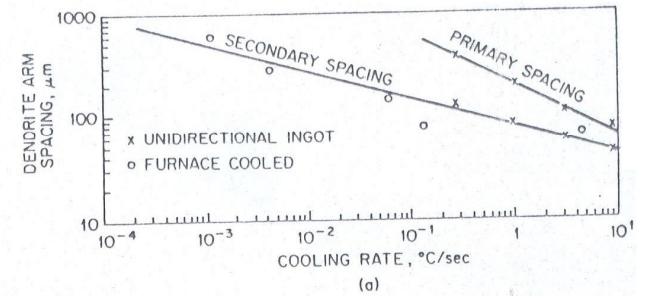


FIGURE 5-15 Some experimental data on dendrite arm spacings in ferrous alloys. (a) Fe-25% Ni alloy (from Flemings et al.¹⁵); (b) commercial steels containing from 0.1 to 0.9% C (from Suzuki et al.²²).

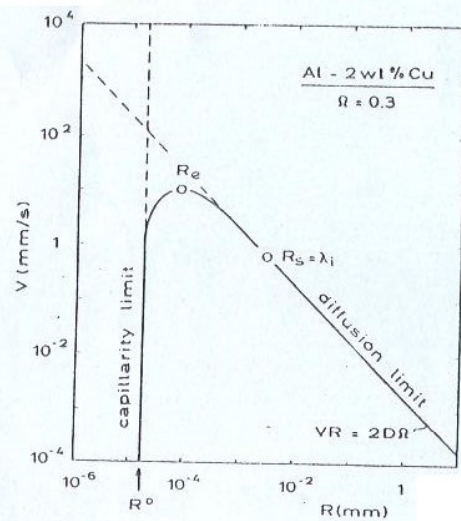


Figure 4.9 Unoptimised Growth Rate of a Hemispherical Needle for $\Omega = \text{Constant}$

For a hemispherical needle crystal, the solution of the diffusion equation shows that the supersaturation, Ω , is equal to the ratio of the tip radius to the characteristic diffusion length. This dimensionless ratio is known as the Péclet number, $P_c (= RV/2D)$. For a given supersaturation, the product, RV , is therefore constant and means that either a dendrite with a small radius will grow rapidly or one with a large radius will grow slowly (diagonal line). At small R -values, the diffusion limit is cut by the capillarity limit. The minimum radius, R^0 , is given by the critical radius of nucleation, r^* (table 2.1). A maximum value of V therefore exists. Because it was reasoned that the fastest-growing dendrites would dominate steady-state growth, it was previously assumed that the radius chosen by the system would be the one which gave the highest growth rate (extremum value, $R = R_e$). However, experiment indicates that the radius of curvature of the dendrite is approximately equal to the lowest wavelength perturbation of the tip, which is close to λ_i (Fig. 3.7). This is referred to as growth at the limit of stability ($R = R_s$).

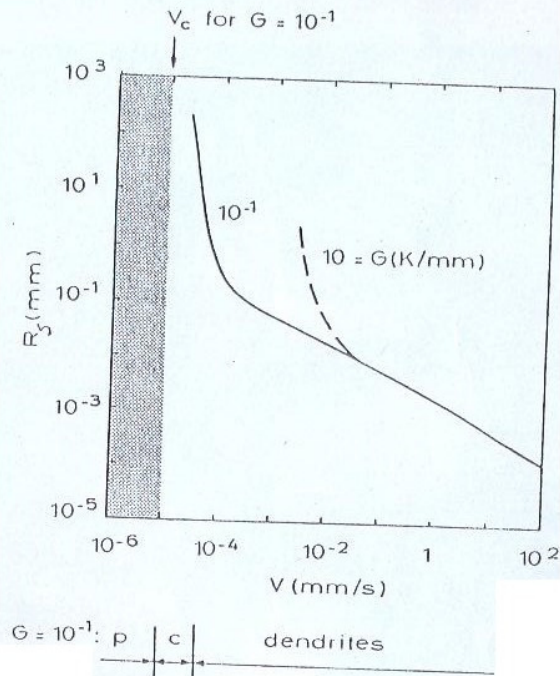


Figure 4.11 Optimised Dendrite Tip Radius as a Function of Growth Rate

If it is assumed that, in directional solidification, growth occurs with a tip radius which is equal to the minimum instability wavelength, λ_i , curves such as those above can be generated. They indicate the marked effect of the temperature gradient upon the radius of curvature at low growth rates (constrained growth regime or cellular (c) regime e.g. for $G = 0.1\text{K/mm}$ between $V = 10^{-4}$ and $V = 10^{-5}\text{mm/s}$). A sufficiently high gradient, or a sufficiently low growth rate ($V_c = GD/\Delta T_0$) will lead to the re-establishment of a planar (p) interface (i.e. a 'dendrite' with an infinite radius of curvature).

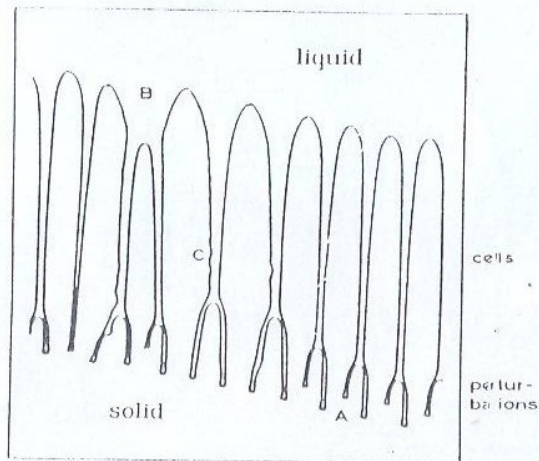


Figure 4.3 Breakdown of a Plane Solid/Liquid Interface to Give Cells

The development of perturbations at the constitutionally undercooled solid/liquid interface (lower part of figure) is only a transient phenomenon. The tips of the perturbations can readily reject solute while the depressed parts of the interface accumulate solute and advance much more slowly. The initial wavelength is too small for further rapid growth to occur, and the final result is the formation of a cellular structure. Note that the wavelength has approximately doubled between the initial perturbation and the final cells. Also, the spacing between the cells is not constant. The initial cellular morphology can adjust itself to give a more optimum growth form via the cessation of growth of some cells (B) in order to decrease their number, or by the division of cells in order to increase the number present. The division of cells is not shown here, but it resembles the change at point A, with two branches continuing to grow. Furthermore, the larger centre cells (C) have slightly perturbed surfaces and this suggests that, in the intercellular liquid, some driving force remains for further morphological change which might possibly lead to dendrite formation.

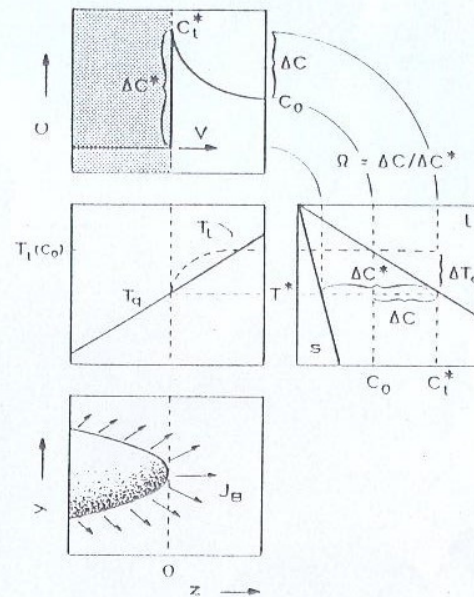


Figure 4.8 Solute Rejection at the Tip of an Isolated Dendrite

During directional solidification, where the isotherms move due to the imposed heat flux, a needle-like crystal can grow more quickly than a flat interface due to the more efficient solute redistribution. Atoms rejected at the interface of a thin needle can diffuse outwards into a large volume of liquid. Thus, the solute diffusion boundary layer, δ_c , of the needle is smaller than that of a planar interface. Also, because the interface is not planar, the solid formed does not have the same composition as the original liquid (as it does in the case of steady-state plane-front growth - Fig. 3.4). When a positive gradient is imposed, as in directional solidification, heat is extracted through the solid. If, furthermore, thermal diffusion is rapid (as in metals) the form of the isotherms will be affected only slightly by the interface morphology. Thus, in the case of directionally solidifying dendrites, *solute diffusion* alone will be the limiting factor. The growth temperature, T^* , of the tip will define a solute undercooling, ΔT_c , or, via the phase diagram, the degree of supersaturation, $\Omega = \Delta C / \Delta C^*$. The determination of Ω as a function of the other parameters requires the solution of the differential equation which describes the solute distribution. The simplest solution is obtained when the tip morphology is supposed to be hemispherical. Instead, the real form of the dendrite tip is closely represented by a paraboloid of revolution.

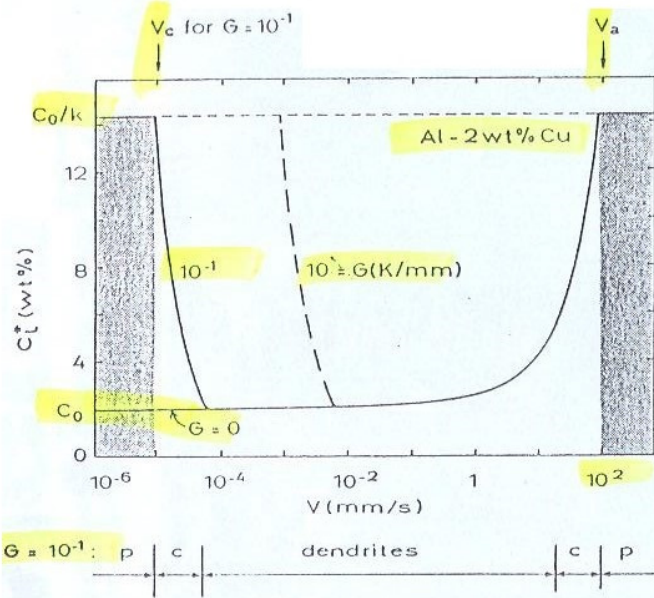


Figure 4.12 Liquid Concentration at the Tip of a Needle Crystal in Directional Growth

From the radius of curvature predicted by figure 4.11, the associated interface concentration can be derived. The blunt cell (c) tips which exist close to the limit of constitutional undercooling, $V_c = GD/\Delta T_0$, cannot easily dissipate the solute rejected there and the tip concentration will therefore be higher than that ahead of a sharp dendrite tip. If the temperature gradient is zero or negative, this will not occur as no cells are formed in this case. At very high growth rates, the interface concentration in the liquid will again increase to high values due to the increase in supersaturation necessary to drive the process. Again, at very high growth rates $V \geq V_a = \Delta T_0 D/k\Gamma$ a crystal with a supersaturation of unity will grow which has the same composition, C_0 , as the alloy (the composition of the liquid at the interface is then equal to C_0/k). Under these conditions, a planar solid/liquid interface (p) will result; as in growth at low rates in a positive temperature gradient (grey regions). Note that the composition of the solid is related to C_l^* via the distribution coefficient, k . The latter becomes a function of V at growth rates of the order of 100 mm/s or above (see chapter 7).

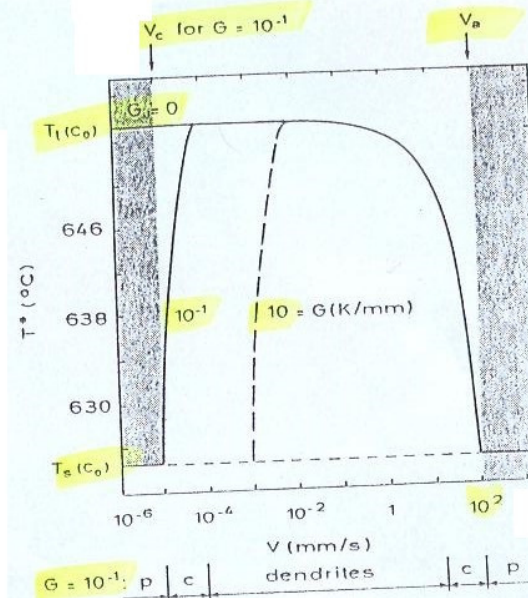


Figure 4.13 Interface Temperature of a Needle Crystal in Directional Growth

Use of the phase diagram and the assumption of the existence of local equilibrium at the solid/liquid interface permit the calculation of the temperature associated with the tip concentration (Fig. 4.12). At high and low growth rates, the tip temperature reaches the solidus temperature. In the low growth rate range, below the critical rate where the dendrite tip temperature and solidus temperature are equal (grey area on the left-hand side), the planar front is the more stable since it can grow at a higher temperature. (This is another way of interpreting the limit of constitutional undercooling). A similar argument applies at high growth rates.

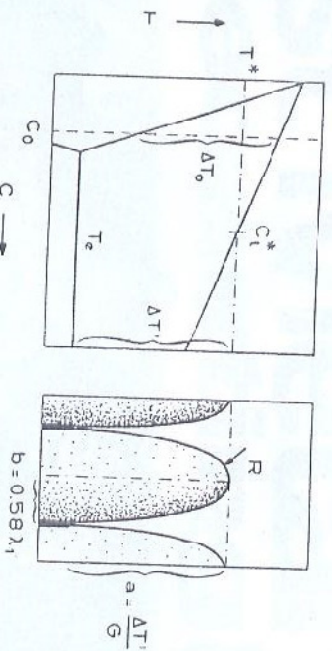


Figure 4.14 Estimation of the Primary Spacing in Directional Solidification

In practical applications, the dendrite tip radius is not as important a parameter as the primary spacing since it is very difficult to measure it directly. However, the tip radius has some influence on the primary spacing. In order to estimate the primary spacing, the dendrites are imagined to be ellipsoidal in shape. The length of the major half-axis, a , of the ellipse is equal to $\Delta T_1/G$. Here, ΔT_1 is the difference between the tip temperature and the melting point of the last interdendritic liquid. The primary spacing, λ_1 , which is proportional to the minor half-axis, b , can be determined from simple geometrical considerations. The factor, 0.58, arises from the assumption that the dendrite trunk arrangement is close-packed hexagonal.

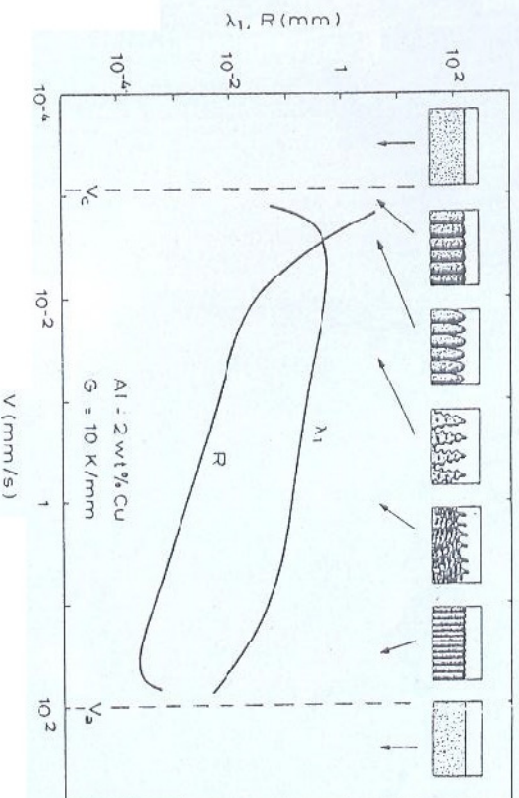


Figure 4.15 Morphology, Tip Radius, and Spacing of Cells and Dendrites

According to the dendrite model, the tip radius decreases from very large values at the limit of constitutional undercooling, V_c to small values at high growth rates (as in figure 4.11). Over the range of dendritic growth, the primary spacing decreases approximately as the square-root of R (equation 4.18). The corresponding interface structures are also shown and vary from planar at growth rates less than V_c to cells and to dendrites which become finer and finer until they give rise to cellular structures again when close to the limit of absolute stability. At V_s , cell solidification structures disappear and again give a planar interface. (For more details on rapid growth, see chapter 7).

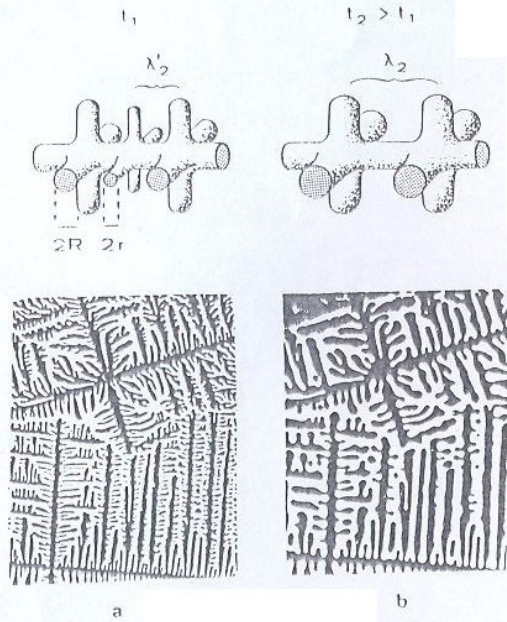


Figure 4.16 Establishment of the Secondary Dendrite Arm Spacing in Equiaxed Solidification

In contrast to the primary spacing, the secondary dendrite arm spacing, as measured in the solidified metal, is largely determined by annealing processes occurring during growth of the dendrites (Fig. 4.6). Due to a ripening phenomenon, smaller (higher curvature) features disappear and 'feed' the growth of the already larger features. The upper figures illustrate the model assumed in calculating the effect of these changes, while the lower photographs show equiaxed cyclohexane dendrites (a) just after solidification, and (b) 20 min later. In these photographs, the black areas correspond to the solid phase and the white areas to the liquid phase. Note that the primary spacing in an equiaxed structure is not well-defined and usually corresponds to the mean grain diameter. [Photographs: K.A.Jackson, J.D.Hunt, D.R.Uhlman, T.P.Seward, Transactions of the Metallurgical Society of AIME 236 (1966) 149].

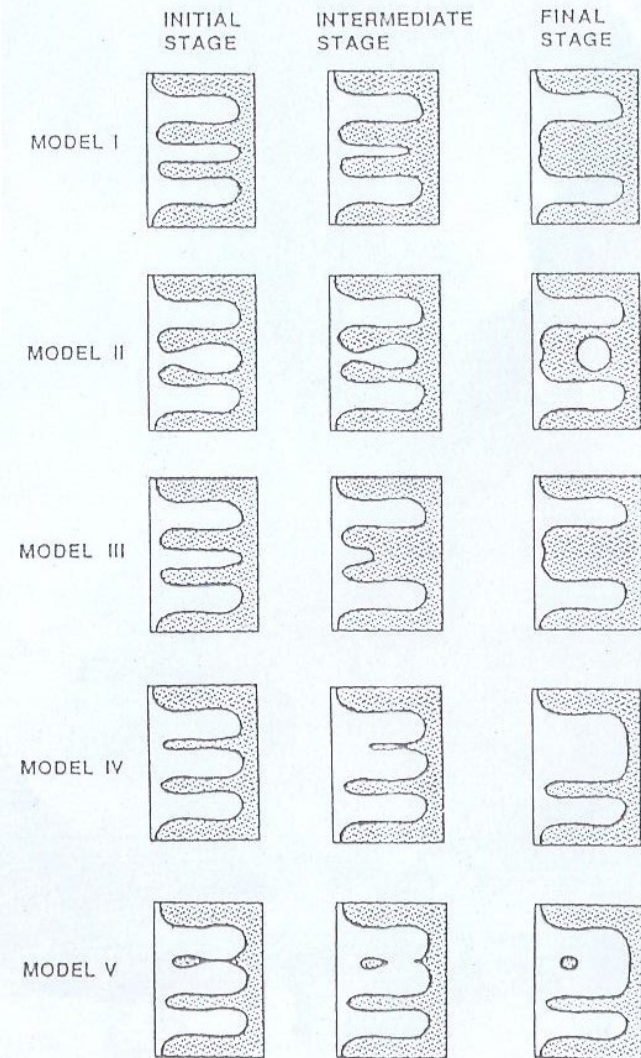


Figure 2-9: Schematic representation of five dendrite coarsening models¹³.

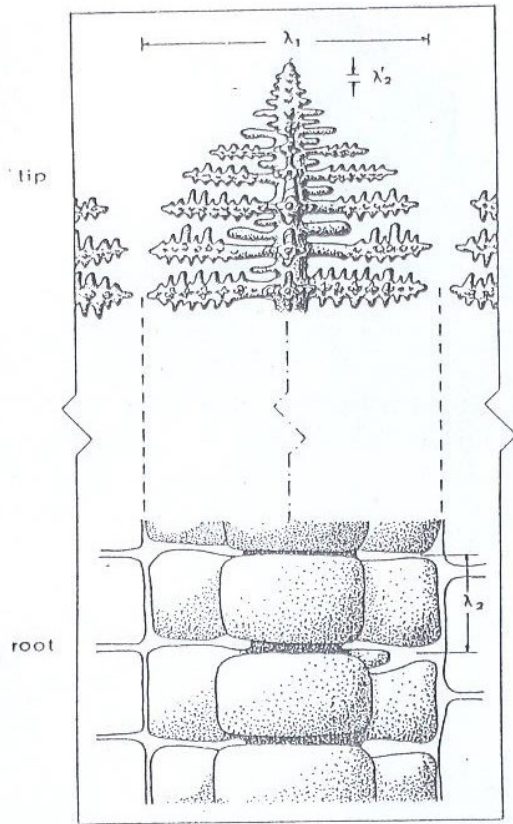


Figure 4.6 Growing Dendrite Tip and Dendrite Root in a Columnar Structure

Depending upon the directional growth conditions, the dendrite (from the Greek, dendron = tree) will develop arms of various orders. A dendritic form is usually characterised in terms of the **primary** (dendrite trunk) spacing, λ_1 , and the **secondary** (dendrite arm) spacing, λ_2 . **Tertiary** arms are also often observed close to the tip of the dendrite. It is important to note that the value of λ_1 measured in the solidified microstructure is the same as that existing during growth, whereas the secondary spacing is enormously increased due to the long contact time between the highly-curved, branched structure and the melt. The ripening process not only modifies the initial wavelength of the secondary perturbations, λ_2' , to give the spacing which is finally observed, λ_2 , but also often causes dissolution of the tertiary or higher order arms. The two parts of the figure are drawn at the same scale, refer to the same dendrite, and illustrate morphologies which exist at the same time but which are widely separated along the trunk length (by about $100 \lambda_1$).

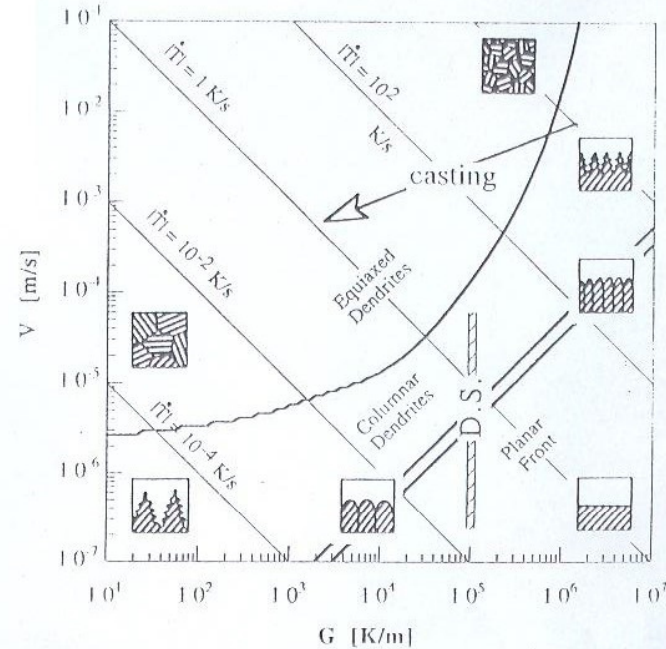


Figure 4.18 Schematic Summary of Single-Phase Solidification Morphologies

This diagram summarises the various microstructures which can be obtained using a typical alloy, with $\Delta T_0=38\text{K}$, when the imposed temperature gradient, G , or growth rate, V , are varied. Provided that a unidirectional heat flow is imposed, the product, $G \cdot V$, is equivalent to the cooling rate \dot{T} , which controls the scale of the microstructures formed. Moving from the lower left to the upper right along the lines at 45° leads to a refinement of the structure for a given morphology. The ratio, G/V , largely determines the growth morphology. Passing from the lower right to the upper left leads to changes in morphology (from planar, to cellular, to dendritic growth). Superimposed on the diagram are typical conditions for two solidification processes, casting and directional solidification (D.S.). The conditions required to produce single-crystal turbine blades (Fig. 4.5) are those at the upper end of the vertical line marked D.S. Processes which produce perfect (homogeneous) single crystals under conditions of plane front growth, such as those required for semiconductor devices (silicon) are found at the bottom of the same vertical line. In a conventional casting, the growth conditions at the solid/liquid interface change with time approximately in the manner indicated upon following the slightly inclined arrow from right to left. The curve indicates the columnar to equiaxed transition for this alloy with $k=0.64$ and a nucleation density and nucleation undercooling of $N_0=4 \cdot 10^{11} \text{ m}^{-3}$ and $\Delta T_n=1.5 \text{ K}$ respectively, Gäumann et al. (1997).

Micro-segregation Length scales

◇ e-Tips
Nr. 14

During solidification, the solid/liquid interface rejects solute into the liquid (we consider here the frequent case when the solubility of the solute element in the solid is smaller than in the liquid). This will always lead to concentration variations in the solidified alloy, known as micro-segregation. The understanding of this phenomenon is the key to interpreting the influence of solidification on the mechanical properties of cast products. Modeling is greatly facilitated by distinguishing between important factors and non-important ones.

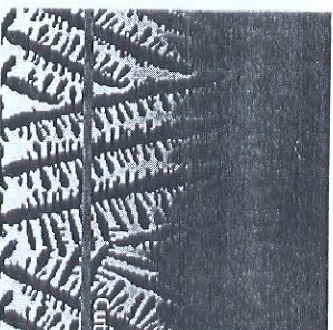


Figure a): Longitudinal representation of growing dendrites

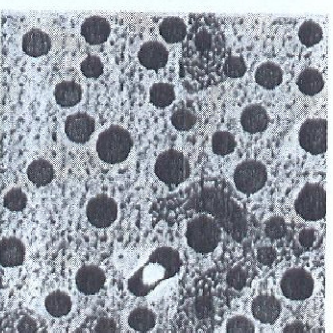


Figure b): Transversal representation of growing dendrites (red line in Figure a).

From Prof. C. Beckermann, Solidification Course 2003, EPFL-Salomon

◇ Case

An Al-2%Cu alloy is solidifying unidirectionally at a constant velocity V_f . The temperature gradient G is imposed by the experimental configuration and we consider for simplicity that there is no flow. The primary dendrite arm spacing is defined as λ_1 .

We will use the values as defined in Table 1 for illustration:

Number	Symbol	Value	Unit	Name
1	V_f	0.1	mm/s	Isotherm speed
2	G	1000	K/m	Thermal gradient
3	k	0.14	-	Equilibrium distribution coefficient
4	m	-2.6	K/wt%	Liquidus slope
5	T_0	650	°C	Melting point of pure Al
6	T_{eut}	574	°C	Eutectic temperature
7	C_0	2	wt%	Alloy concentration
8	C_{eut}	33.1	wt%	Eutectic concentration
9	λ_1	500	μm	Primary dendrite arm spacing
10	D_1	$3 \cdot 10^9$	m^2/s	Diffusion coefficient in liquid
11	D_s	$3 \cdot 10^{12}$	m^2/s	Diffusion coefficient in solid
12	α	$3.7 \cdot 10^5$	m^2/s	Thermal diffusivity

Table 1:

Values 1-2, 9 are given by the experiment,

they should be measured.

Values 3-5, 8 are given by the phase diagram of the Al-Cu system.

Value 7 is an input of the problem.

Values 10-12 should be found in reference book1.

Results

1) Liquidus temperature, T_L

The liquidus temperature can be calculated as follow:

$$T_L = T_0 + m \cdot C_0 = 654,8 \text{ }^\circ\text{C}$$

2) Mushy zone length, L_M

The mushy zone length can be calculated as follow:

$$L_M = (T_L - T_{\text{tip}}) / G = 0,0808 \text{ [m]} \\ = 8,08 \text{ [cm]}, \text{ not so small!}$$

3) Local solidification time, t_s

The local solidification time can be calculated as follow:

$$t_s = L_M / V = 808 \text{ [s]} = 13,5 \text{ minutes}$$

4) Mean transversal speed of the solid/liquid interface in Figure b), V_I

The mean speed of the s/l interface in view b) can be calculated as follow:

$$V_I = (\lambda/2) / t_s = 3,1 \cdot 10^{-7} \text{ [m/s]} \\ = 0,3 \text{ } \mu\text{m/s} \ll V_L$$

The transversal growth speed is much smaller than the longitudinal growth rate.

5) Estimation of the thermal and solutal diffusion lengths in the liquid (Figure b)

$$L_{\text{thermal}} = \alpha / V_L = 1,9,7 \text{ [m]} \gg \lambda \\ L_{\text{solutal}} = D_L / V_L = 9,7 \text{ [m]} \gg \lambda$$

This means that the temperature in the liquid can be considered as uniform as well as the concentration (complete mixing). Note that the thermal diffusion length is 10'000 larger than the solutal one.

6) Estimation of the thermal and solutal diffusion lengths ahead of the primary dendrite tips

$$L_{\text{thermal}} = \alpha / V_L = 0,37 \text{ [m]} \gg \lambda \\ L_{\text{solutal}} = D_L / V_L = 2 \cdot 10^{-5} \text{ [m]} \ll \lambda$$

The solutal gradient ahead of the primary dendrite tips cannot be neglected.

7) Estimation of the characteristic solutal diffusion times in the liquid and solid on the scale of dendrite arm spacing (Figure b))

$$t_{\text{liquid}} = (\lambda/2)^2 / D_L = 20,8 \text{ [s]} \ll t_s \\ t_{\text{solid}} = (\lambda/2)^2 / D_S = 2 \cdot 10^5 \text{ [s]} \gg t_s$$

This means that there is enough time to smooth concentrations profiles in the liquid while this is not the case in the solid, i.e. a gradient in the solid will be present after solidification.

8) Estimation of the characteristic solutal diffusion time in the liquid over the length of the mush

$$t_{\text{liquid}} = (L_M)^2 / D_L = 2,2 \cdot 10^6 \text{ [s]} \gg t_s$$

This means that solutal diffusion in the liquid parallel to dendrites can be neglected because the characteristic time is much greater than the solidification time

Conclusion

Knowing the importance of the these "orders of magnitude" influences on solidification can help us to distinguish between important factors and less important factors. These can then help us develop more simplified, but realistic, computer models of solidification phenomena while saving a lot of calculation time.

